ELECTROMAGNETIC-THERMAL MODELING FOR HIGH-FREQUENCY AIR-CORE PERMANENT MAGNET MOTOR OF AIRCRAFT APPLICATION

BY

XUAN YI

THESIS

Submitted in partial fulfillment of the requirements
for the degree of Master of Science in Electrical and Computer Engineering
in the Graduate College of the
University of Illinois at Urbana-Champaign, 2016

Urbana, Illinois

Adviser:

Associate Professor Kiruba Sivasubramaniam Haran

ABSTRACT

A 1 MW high-frequency air-core permanent-magnet (PM) motor, with power density over 13.8 kW/kg (8 hp/lb) and efficiency over 96%, is proposed for NASA hybrid-electric aircraft application. In order to maximize power density of the proposed motor topology, a large-scale multi-physics optimization is needed to obtain the best design candidates, which is not favorable for current electrical machine software. Therefore, developing electromagnetic (EM) and thermal analytical methods with computational efficiency and decent accuracy is a key enabling factor for future multi-physics optimization of motor power density.

In this thesis, the detailed development process of electromagnetic analytical modeling for the proposed machine will be presented and verified with finite element analysis (FEA). Corresponding heat loads, including electrical and mechanical losses, will be quantified rigorously to assess efficiency and prepare for the following thermal analysis. Furthermore, accurate physical-thermal conductivities of different machine components are required to eliminate uncertainties in thermal performance prediction. One arising challenge is to quantify the equivalent thermal conductivity of a complicated composite component — the winding — which is also the most critical one regarding overheating risks. Detailed methods of quantifying winding equivalent thermal conductivity will be presented, discussed, and verified with a bench test. The last step in EM-thermal modeling is using a simplified thermal equivalent circuit to quickly detect hotspot temperature and therefore to eliminate infeasible machine designs efficiently. Similar to EM modeling, rigorous thermal analytical modeling will be presented and verified with FEA results.

To my parents, for their love and support.

ACKNOWLEDGMENTS

Above all, I would like to thank my parents for their endless love, support and encouragement.

I would like to express my deep gratitude to my adviser, Dr. Kiruba Haran, for his continuous support and patience of my master degree's study and research. His immense knowledge and insightful guidance in electrical machine technology helped my mind grow. I would also like to thank Dr. Arne Pearlstein for his guidance and suggestions on my thermal analysis work.

In addition, I would like to thank my colleagues, Digvijay Deswal and Jon Martin, for their help and suggestions on my thermal conductivity measurement bench test. Also, thank you to Andy Yoon for his help on the electromagnetic modeling in electrical machine design software.

Last, I would like to express my gratitude to the Grainger Center for Electric Machinery and Electromechanics (CEME), and the National Aeronautics and Space Administration (NASA) for their financial support.

TABLE OF CONTENTS

CHAPTER 1

INTRODUCTION

1.1 Background

In order to satisfy relentless growth in air traffic and achieve fuel efficiency while minimizing environmental damage, electric aero-propulsion has been proposed as one of the solutions for aviation industry challenges. Aircraft electrification basically can be implemented by replacing conventional engine and fossil-fuel sources with electric motor and batteries. Despite recent developments in battery storage technologies, the jet fuel energy density at 46 MJ/kg is still twice the current state-of-the-art of battery storage energy density. Therefore, full electrification of airplanes is not favored currently.

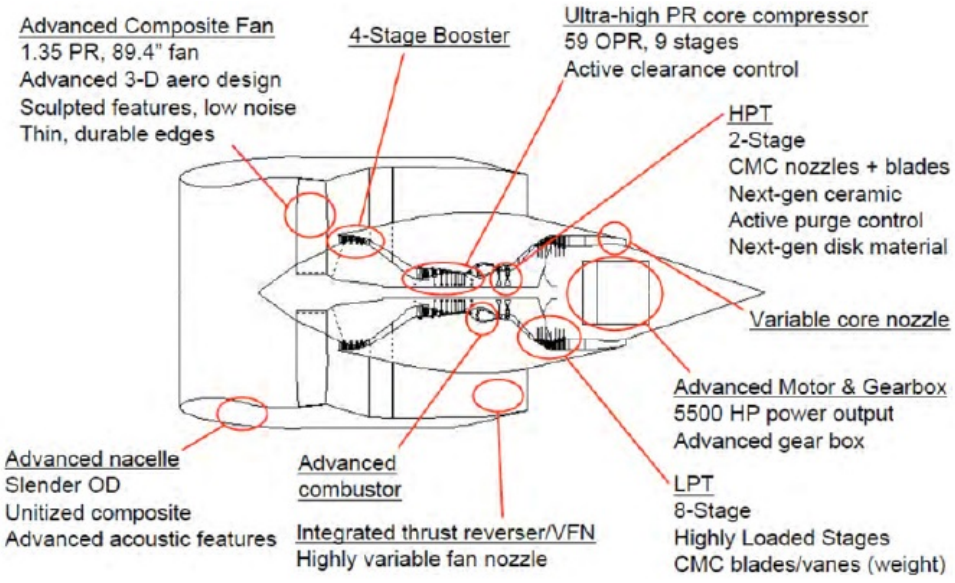

Figure 1.1: Illustration of Turbo-electric Propulsion System [1]

However, an interim solution is a hybrid gas-electric concept benefiting from both fossil fuels and batteries. The electric motor replaces the conven-

tional jet engine and directly drives turbo fans as illustrated in Figure 1.1. The power density of the electric motor, as a key enabling factor of hybrid-electric airplane technology, needs to be at least 2–4 times that of the state-of-the-art [2].

It has been theoretically proven that superconducting machines can power electric airplanes to carry hundreds of people. These machines apply superconducting technology to produce dramatically high flux density and high current density, and thus can significantly reduce weight/volume [3]. However, a complex cooling system, such as a cryogenic one, is required to provide a critical operating environment for superconducting materials. Failures of superconducting machines due to lack of critical operating environment could result in significant risks for aircraft applications.

In parallel with research in superconducting machine design for aircraft applications, research in conventional electrical machines seeks ways to boost power density. Conventional machines do not require complicated cooling systems (cryogenic, etc.) and suffer fewer operating failures than superconductor machines. Some conventional machine typologies, such as surface permanent magnet machines, are candidates for achieving high power density. For aircraft applications, conventional machines must reach a power density of 8 hp/lb (four times than the existing state-of-the-art) to produce similar results.

1.2 Motivation

A 1 MW non-cryogenic, high-frequency, high-pole-count and high-speed air-core permanent magnet motor is proposed for achieving goals of NASA for future hybrid-electric aircraft applications. The proposed motor needs to reach at least 13.6 kW/kg (8 hp/lb) power density and 96% efficiency shown in Figure 1.2. As a reference, the current highest power density of an air-cooled PM motor is approximately 2.6 hp/lb rated to 20 kW for electric vehicle applications [4].

High machine power density can be achieved by maximizing output power but minimizing weight during the design process. Output power maximization highly depends on available magnetic loading, electric loading, rotor volume and rotating speed, which are constrained by physical and multidis-

Figure 1.2: Electric Machine Development Roadmap for Aircraft Electrification [5]

ciplinary principles including electromagnetic, thermal and mechanical perspectives. With advances in material, thermal management, and structural integrity technologies, the output power factors can be improved significantly. Weight reduction is determined by topology and structure design. In the electrical machines, iron, permanent magnet, and copper are the densest materials. How to minimize use of heavy materials while maintaining sufficient output power is the key to high-power-density machine design. The correlation of determinants of machine power density cannot be investigated without analytical modeling development.

Another aspect of maximizing the power density of machines is to mathematically optimize machine size with given specifications. In electrical machine design, most people use finite-element analysis (FEA) to predict electrical and thermal performance. Even though such analysis can accurately predict machine performance, it is too complicated, time-consuming, and inflexible to varying design cases and running large-scale design optimization.

The goal of this thesis is to develop analytical electromagnetic and thermal modeling of proposed machine topology to facilitate power density optimization. Also, such analytical solutions can provide physical insights and computational efficiency when sizing electrical machines and assessing design feasibility.

The insights of electromagnetic-thermal correlations in electrical machine design will be presented and discussed. Detailed derivations of electromagnetic and thermal modelings for proposed machine topology will be presented, and their accuracy will be assessed. Quantification methods of key thermal analysis parameters, including electrical and mechanical losses, and Litz wire equivalent thermal conductivity, will be presented and discussed. A thermal

bench test was conducted to verify quantification methods for eliminating partial prediction uncertainties.

CHAPTER 2

MACHINE STRUCTURE DESIGN & REQUIREMENTS

Machine sizing is the core factor in machine designs. The first-order machine sizing relation with output power is presented as follows [6]:

$$P_{out} = w_m V_{rotor} k_w K_{s(rms)} B_{gm(rms)} \eta_{gap} \tag{2.1}$$

Rotating speed (w_m), rotor volume (V_{rotor}), magnetic loading ($B_{gm(rms)}$), and electric loading ($K_{s(rms)}$) are the first-order determinations in specific power that an electric machine can reach. Efficiency and losses are the second-order factor in machine design, which usually results from the first-order determinations. The third order factor is the winding, which is usually determined by the winding patterns, pole-slot relations and slot shapes.

With defined rotor volume, there are several ways to increase the power density of a machine. On the one hand, the machine weight needs to be minimized by utilizing lightweight materials and cutting off heavy metals, such as iron. On the other hand, the machine output power needs to be maximized by maintaining high magnetic loading, electric loading and rotating speed.

However, none of these ways to boost power density is perfect, due to material physical properties. Magnetic loading, also referred to as fundamental gap flux density, depends on magnetic volume, magnetic property gap thickness, and yoke thickness. Electric loading is mainly constrained by the capability of thermal management. Rotor speed is limited by structural integrity. For a PM machine, a high-strength retaining ring material is required to safely confine magnets during rotation. Aggressive cooling techniques and advanced materials are used in high-power-density machines to maintain high electromagnetic loadings and high speed.

2.1 Machine Topology

In this proposed high-power-density machine for aircraft electrification propulsion system, air-core and high-frequency high-pole-count typologies are applied. The proposed motor configuration is shown in Figure 2.1.

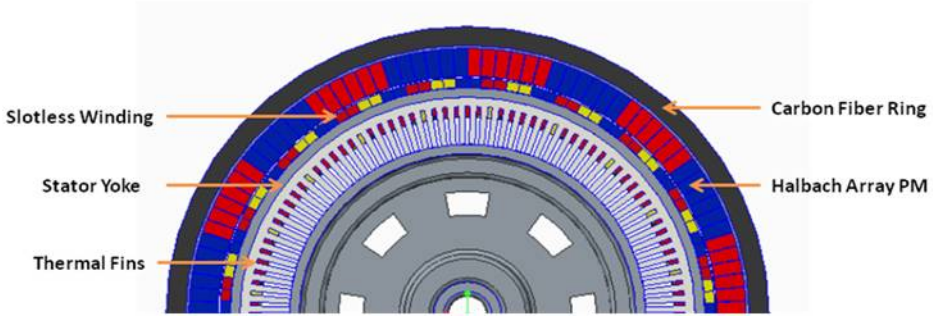

Figure 2.1: Illustration of Machine in the Cross Section View

2.1.1 Air Core Topology

Traditional electrical machines often use a large amount of heavy metal—iron to conduct magnetic flux through the gap and windings. Therefore, they tend to be heavy and have low power density. Also, iron teeth tend to see a large amount of core losses at high frequency operation and saturation effects. Therefore, slotless topology is employed to reduce machine weight significantly and avoid potential high core loss by removing teeth with slotless winding (airgap winding). Slotless winding has advantages of more electric loading, less core loss, and low torque ripples. Lower torque ripples can reduce the risks of unstable vibrations and rotor eccentricity. But the disadvantage of using slotless winding is less flux coupling capabilities, which poses challenges of maintaining the high magnetic loading requirement.

One method to maintain decent magnetic loading is using a Halbach array permanent magnet. Basically, this topology uses a magnet array pattern to follow the flux path direction illustrated in Figure 2.2. Correspondingly, magnetic flux can be enhanced on one side of array, but weakened or eliminated on the other. With Halbach array, the backside of magnet does not require an iron yoke in the rotor, and gap flux density can be improved even with slotless windings.

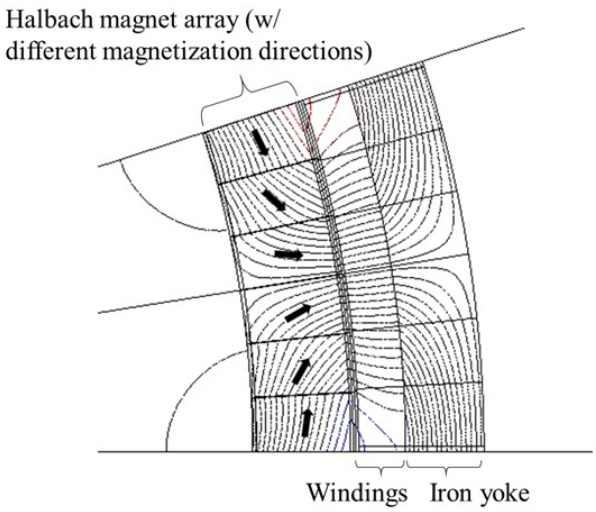

Figure 2.2: Halbach Magnet Array Flux Path in Electrical Machine [7]

The other method is using outer-rotor topology. Since a retaining ring is required to prevent magnet arrays from flying apart, it causes more effective gap thickness and more magnetic reluctance in the gap flux path. Instead of keeping the retaining ring in the gap, it can be moved out of the gap by applying outer-rotor topology. Thus, the gap thickness can be minimized in this way and magnetic loading is improved further.

2.1.2 High-Frequency High-Pole-Count Topology

Even though eliminating teeth and rotor back-yoke saves a significant amount of weight, stator back-yoke size can be reduced further by applying high-pole-count topology. The thickness of stator back-yoke is proportional to magnetic flux per pole (Φ_p). More flux per pole requires more iron material to conduct due to magnetic saturation effects. With fixed rotor volume and magnetic loading, flux per pole is inversely proportional to pole number according to the following:

$$\Phi_p = \frac{2V_{rotor}B_{g1}}{P} \tag{2.2}$$

It indicates that stator iron yoke thickness can be reduced further by raising the pole number shown in Figure 2.3. But the challenge of high-pole-count topology is the associated high electrical frequency. High electrical frequencies might causes more iron losses, because iron losses increase quadratically

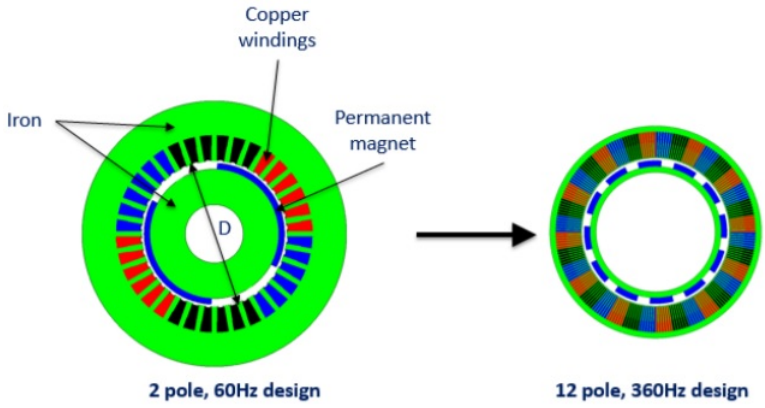

Figure 2.3: 2-Pole and 12-Pole Motor Design 2D EM FEA Model [8]

with frequency.

The last factor that can boost machine power density is rotating speed (w_m). Rotating speed is highly related to the structural integrity. In this design, super high-strength material, carbon fiber ring, is employed to confine permanent magnet array in the rotor during high rotating speed. In addition, the bearing design is very challenging due to critical vibration modes and severe radial expansions in the gap at high speed.

2.2 Thermal Management

Electric loading plays a significant role in deciding the machine specific power. Unfortunately, it cannot be raised to infinitely large value, because induced conduction loss in the windings drives hotspot temperature beyond the material thermal limit. Usually, the machine temperature limitation is determined by the winding insulation material. The maximum temperature of winding insulation could range 100 to 250 °C in conventional machines. Therefore, maximum allowable electric loading in the machine design really depends on the capability of thermal management.

In thermal management, two important things need to be considered. One is to keep losses as low as possible, especially key components, like windings and iron yoke. Due to the limited motor space/weight, several percentage points of rated power lost to heat can result in significantly high heat flux density. The other is to maximize cooling capability. All machine losses are required to be removed effectively, and reducing thermal resistances in

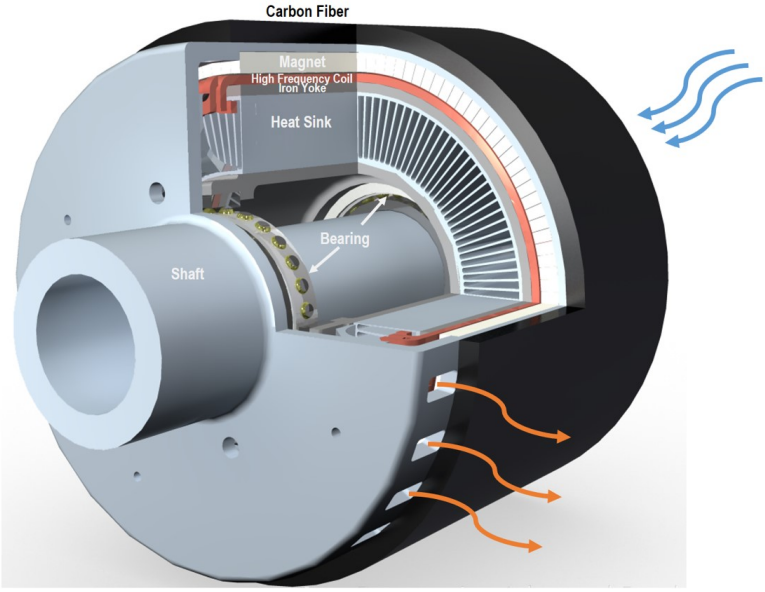

Figure 2.4: 3D View of Proposed High-Power-Density Motor for Hybrid-Electric Aircraft

the thermal conduction path lowers hotspot temperature. In other words, aggressive and advanced cooling techniques are the key to raising machine power density.

The cooling method in this machine design is an aggressive self-pumped air cooling, which does not require any extra components added to machine weight, other than fan blades. The cooling flow is expected to go through the gap and cooling channels to take out mechanical and electrical losses, as indicated by Figure 2.4. A centrifugal fan is attached at the front rotor region. While the rotor spins, cooling flow will be sucked into the motor and released at outlet holes on the rotor outer surface.

The challenges of such a cooling scheme are complicated aerodynamic analysis, fan design and effective heat conduction method. Air is not a good heat conductor or heat capacitor, so a large amount of axial cooling air flow is needed to remove the heat from the motor quickly before the air temperature saturates. Additionally, sufficient heat transfer coefficient can allow large heat flux density coming out of the machine. Cooling capability also relies on the cooling speed on the solid/gas surface and coolant temperature. Thus, both adequate mass cooling flow and effective heat transfer are essential for achieving a high-power-density motor.

Another important factor in thermal management is the conduction effect.

The motor hotspot temperature is generated in the solid component with heat losses and then lost heat can be conducted through different solid components until reaching the cooling flow boundary. The previous paragraph only focuses on heat transfer effects, more related to flow dynamics. Heat conduction mainly happens among solid parts. In this motor, the winding is sitting on top of the stator yoke, and a heat sink is attached underneath the stator yoke. Since a huge amount of windage loss and insufficient axial cooling flow in the gap, the only effective heat conduction path for the winding (with significant amount of copper losses and electric loadings) is through the cooling channels. Unfortunately, windings are not made of pure copper which can conduct heat effectively. Several layers of electric insulation are embedded to reduce bundle eddy current losses and to avoid break-down voltage and short-circuits. How to quantify and improve winding equivalent thermal conductivity is crucial in evaluating and lowering motor hotspot temperature.

CHAPTER 3

ELECTROMAGNETIC ANALYSIS

Electromagnetic analysis is a primary step in machine design that determines primary machine performance. The finite-element method is broadly used by current machine design commercial software. However, such method does not provide geometry variation flexibility of this specific novel machine topology for electric aircraft application. If a large-scale optimization of machine performance needs to be carried out, it is rather tedious to modify geometry parameters, especially for complicated design. Another disadvantage of using FEM is that it is computationally time-consuming. It has to evaluate every node point value of the automatically generated mesh and involves a large matrix calculation with thousands to millions of entries. For a small number of design cases, total evaluation time is not sensible, maybe merely several seconds. But if the design cases accumulate, total evaluation time will increase linearly and ends up at hours or days. To avoid heavy computations with FEM, an accurate analytical EM model derived from fundamental Maxwell's equations is employed in this work.

3.1 Electromagnetic Analytical Model

The EM analytical model is divided into three regions and bounded with the infinite permeable material shown in Figure 3.1. Region 1 is the outside region of the Halbach PM array. Region 2 is the Halbach PM array. Region 3 is the air gap and slotless winding in the stator.

The machine magnetic field is predicted based on the following assumptions:

1. The Halbach array is assumed to form a perfect sinusoidal magnetic waveform in the air gap.

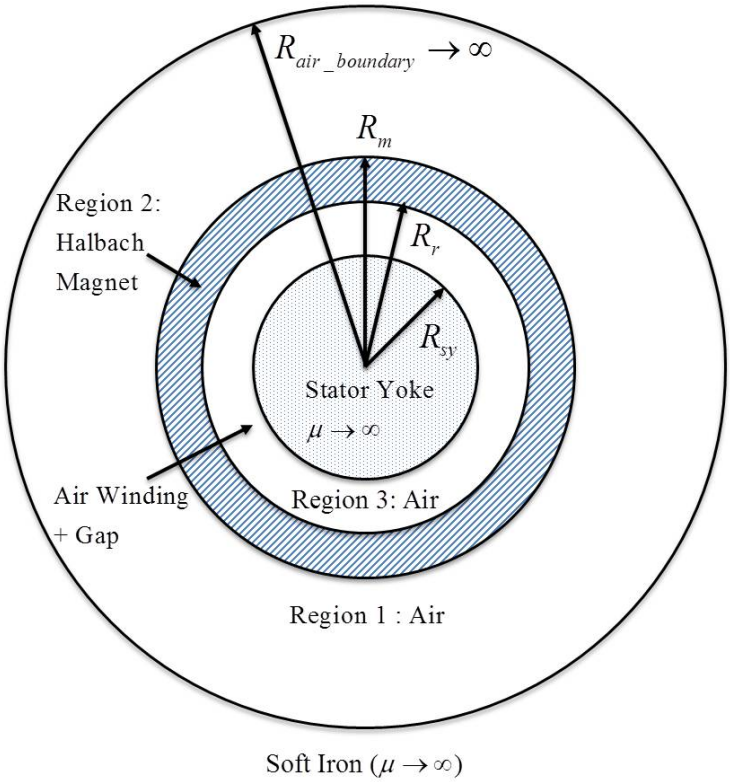

Figure 3.1: Illustration of EM Analytical Model

2. The back yoke permeability in the stator is regarded as infinite to simplify the problem.

3. Harmonics are ignored here, since they do not contribute to the average torque and their amplitude is negligible compared with the fundamental.

The EM analytical model arises from Maxwell's equations. In electrical machines, EM waveform frequency is fairly low and no displacement current occurs. It is usually treated as a magneto-static problem. And following are governing equations in the electrical machine EM analytical model:

$$\nabla \times \vec{H} = \vec{J} \tag{3.1}$$

$$\nabla \cdot \vec{B} = 0 \tag{3.2}$$

For non-magnet regions, the magnetic flux density and flux intensity relation can be written as

$$\vec{B} = \mu_o \mu_r \vec{H} \tag{3.3}$$

For magnet regions, there is extra magnetic flux density contributed by permanent magnet material, since permanent magnet material possesses remanent flux and does not require a current source to produce magnetic flux. Therefore, magnetic flux density and flux intensity relation with permanent magnet effects yields

$$\vec{B} = \mu_o \mu_r \vec{H} + \mu_o \vec{M} \tag{3.4}$$

The magnetization distribution $\vec{M}$ varies sinusoidally along the rotor angle θ and is given by

$$\vec{M} = M\cos(p\theta)\hat{r} + M\sin(p\theta)\hat{\theta} \tag{3.5}$$

where M is defined as B_{rem}/μ_o.

Since this is an open-circuit magnetic flux analysis, the current density in the winding region is zero. That means the rotation part of magnetic flux intensity vector $\vec{H}$ is zero and only the gradient part exists. Therefore, a magnetic scalar potential (Φ_M) can be employed here:

$$\vec{H} = -\nabla \Phi_M \tag{3.6}$$

And tangential and rotational components of magnetic fields can be obtained from scalar magnetic potential as

$$\vec{H_r} = \frac{\partial \Phi_M}{\partial r} \tag{3.7}$$

$$\vec{H_\theta} = -\frac{1}{r}\frac{\partial \Phi_M}{\partial \theta} \tag{3.8}$$

For the magnet region, magnetic potential Poisson's equation can be derived as

$$\nabla \cdot \vec{B} = \nabla \cdot (\mu_o \mu_r \vec{H} + \mu_o \vec{M}) = 0 \tag{3.9}$$

$$\nabla^2 \Phi_M = \frac{\bigtriangledown \cdot \vec{M}}{\mu_r} \tag{3.10}$$

Similarly, for the non-magnet region, magnetic potential Poisson's equation is

$$\nabla^2 \Phi_M = 0 \tag{3.11}$$

Poisson's equation is a partial differential equation frequently utilized in theoretical physics. It describes the potential field induced by a magnetic or electric source. In this example, it can be defined as

$$\bigtriangledown^2\Phi_M = \frac{\partial^2\Phi_M}{\partial r^2} + \frac{1}{r}\frac{\partial\Phi_M}{\partial r} + \frac{1}{r^2}\frac{\partial^2\Phi_M}{\partial\theta^2} = f(r,\theta,z,M,\mu) \tag{3.12}$$

The general solution of Equation 3.12 is the sum of the homogeneous solution and particular solution as

$$\Phi_M = \Phi_{M\_homogeneous} + \Phi_{M\_particular} \tag{3.13}$$

The arbitrary homogeneous solution accordingly is

$$\Phi_M(r,\theta) = a_0 + b_0 ln(r) + \sum_{k=1}^{\infty}[(A_k r^k + B_k r^{-k})\cdot(C_k cos(k\theta) + D_k sin(k\theta)] \tag{3.14}$$

Only excitation frequency of the magnetic source can induce magnetic waveforms in the machine. In this calculation, only the fundamental frequency is considered. The DC and other frequency components in Equation 3.14 can be ignored accordingly.

Region 1 and region 3 fall into the homogeneous Poisson's equation and do not require a particular solution. However, a particular solution is required in region 2 (magnet region) and yields

$$\Phi_{M2\_particular} = \frac{M}{\mu_r}\frac{r}{1-p}cos(\theta) \tag{3.15}$$

which satisfies the region 2 governing equation.

The boundary conditions at $R = R_{air\_boundary}$ and $R = R_{sy}$ yield

$$H_\theta = 0 \tag{3.16}$$

Continuous boundary conditions can be applied at other boundary interfaces among different regions. Both the tangential component of $\vec{H}$ and radial component of $\vec{B}$ are continuous across different arbitrary media 1 and media 2 shown as

$$H_{\theta\_media1} = H_{\theta\_media2} \tag{3.17}$$

$$B_{r\_media1} = B_{r\_media2} \tag{3.18}$$

With given boundary conditions and known magnetic sources, simplified general solutions for Poisson's equation of magnetic scalar potential can be

derived as

$$\Phi_{M1} = (A_1 r^p + B_1 r^{-p}) cos(\theta) \tag{3.19}$$

$$\Phi_{M2} = (A_2 r^p + B_2 r^{-p} + \frac{M}{\mu_r} \frac{r}{1-p}) cos(\theta) \tag{3.20}$$

$$\Phi_{M3} = (A_3 r^p + B_3 r^{-p}) cos(\theta) \tag{3.21}$$

The unknown coefficients in Equation 3.19 to 3.21 can be solved with coupled boundary conditions, and thus a magnetic flux density analytical solution in all the defined regions in Figure 3.1 can be derived. According to [9], the magnetic flux density solutions in the slotless winding region (Region 3) are given as:

$$B_r(r,\theta) = \frac{4B_{rem}}{D_0} \frac{p}{1-p} (1+\mu_r) \left[1 - \left(\frac{R_r}{R_m} \right)^{p-1} \right] \left[1 + \left(\frac{R_{sy}}{r} \right)^{2p} \right] \left(\frac{r}{R_r} \right)^{p-1} cos(p\theta) \tag{3.22}$$

$$B_\theta(r,\theta) = -\frac{4B_{rem}}{D_0} \frac{p}{1-p} (1+\mu_r) \left[1 - \left(\frac{R_r}{R_m} \right)^{p-1} \right] \left[1 + \left(\frac{R_{sy}}{r} \right)^{2p} \right] \left(\frac{r}{R_r} \right)^{p-1} sin(p\theta) \tag{3.23}$$

$$D_0 = 2(1-\mu_r) \left[(1-\mu_r) \left(\frac{R_r}{R_m} \right)^{2p} + (1+\mu_r) \left(\frac{R_{sy}}{R_m} \right)^{2p} \right] - 2(1+\mu_r) \left[(1+\mu_r) + (1-\mu_r) \left(\frac{R_{sy}}{R_m} \right)^{2p} \right] \tag{3.24}$$

where μ_r is permanent magnet permeability, p is pole pair number, R_r is rotor inner radius, R_m is magnet outer radius, and R_{sy} is stator yoke outer radius shown in Figure 3.1.

Slot current density (J_{s_rms}) is assumed to be uniformly distributed across the whole slotless winding region. The Lorentz force can only be generated

when magnetic flux is perpendicular to current. And current is flowing in the axial direction. So only radial component of magnetic flux density contributes to electrical force. Overall, average electrical torque (T_e) can be determined with Lorentz force definition

$$T_e = \iiint_V B_r J_{s\_rms} \; dr \; d\theta \; dz \tag{3.25}$$

where V is total slotless winding volume. The final result of average torque can be derived from Equations 3.22 - 3.25 as

$$T_e = \frac{4\pi B_{rem} J_{s\_pk} L}{D_0} \frac{p}{1-p}(1+\mu_r)\left[1-\left(\frac{R_r}{R_m}\right)^{p-1}\right] \left[\frac{1}{p+2}\frac{R_w^{p+2}-R_{sy}^{p+2}}{R_r^{p-1}} + \frac{1}{2-p}\frac{R_{sy}^{2p}}{R_r^{p-1}}\left(R_w^{-p+2}-R_{sy}^{-p+2}\right)\right] \tag{3.26}$$

where B_{rem} is remnant magnetic flux density, J_{s_pk} is slot peak current density, L is active length of machine, R_w is winding outer radius.

Since iron is one of heaviest materials used in electrical machines, quantifying iron yoke volume/thickness is important to evaluating machine overall weight correlated with magnetic loading. Minimum stator yoke thickness (d_{sy}) can be derived from the flux distribution analytical solution. The according equation can be derived as

$$d_{sy} = \frac{R_{sy}}{p}\frac{B_{r\_sy}}{B_{sat\_sy}} \tag{3.27}$$

where B_{r_sy} is radial flux density at $r = R_{sy}$ evaluated in Equation 3.22, and B_{sat_sy} is stator yoke saturation flux density.

3.2 Verification with Finite Element Analysis

After deriving the detailed magnetic analytical model, the accuracy of the method needs to be confirmed within a decent range to eliminate uncertainty concerns. At the current stage, no prototype of the proposed machine topology has been built. The only way to verify the magnetic analytical solution is to adopt finite element analysis, which is widely used by most machine design software. Primary baseline design machine dimensions and key pa-

Table 3.1: Primary Baseline Design Machine Metrics

Magnet outer radius	R_m	0.152	m
Rotor inner radius	R_r	0.138	m
Winding outer radius	R_w	0.137	m
Stator yoke inner radius	R_{sy}	0.132	m
Active length	L	0.213	m
Gap thickness	δ	0.001	m
Pole pair number	p	10	
Magnet remnant flux density	B_{rem}	1.20	T
Magnet permeability	μ_r	1.04	

rameters are offered in Table 3.1. A professional electrical machine design software—Flux—is utilized to verify design feasibility theoretically. With the given baseline design dimensions, detailed flux distribution is shown in Figure 3.2 by applying the finite element method in Flux 2D. It indicates that flux is confined very well on the rotor side due to the characteristic of the Halbach PM array. Also, in the gap and winding region, flux magnitude can be maintained around 0.95 to 1 Tesla although no yoke teeth exist to conduct flux.

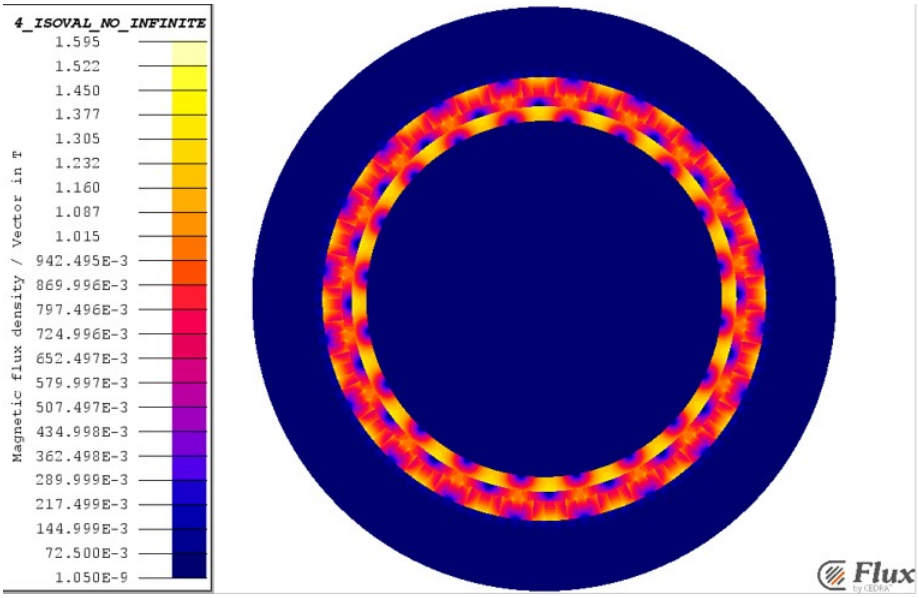

Figure 3.2: FEA Contour Plot of Flux Density Distribution in Motor

All the results of the established EM model strongly agree with the FEA results. Given the primary design metrics listed in Table 3.1, the open-circuit magnetic fields of the analytical solution exactly match the FEA shown in

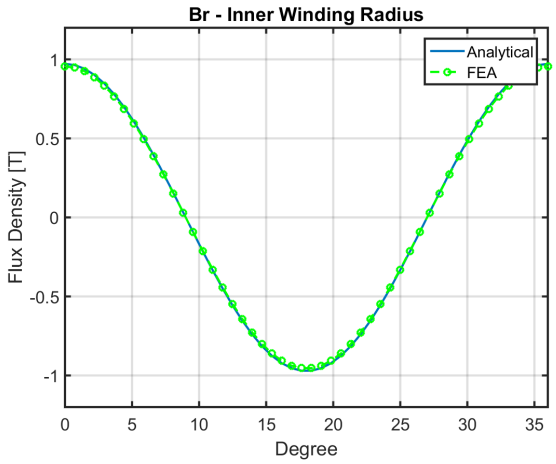

(a) Inner Winding Radius

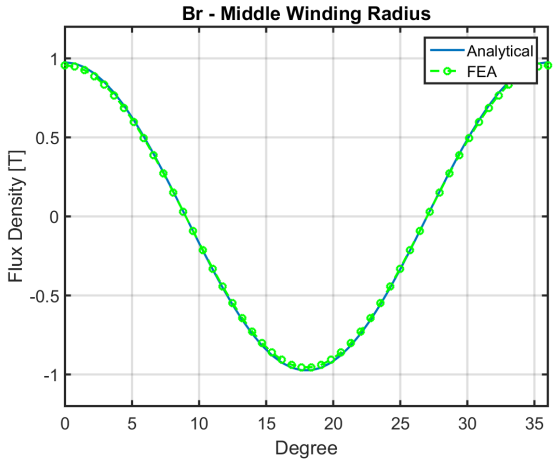

(b) Middle Winding Radius

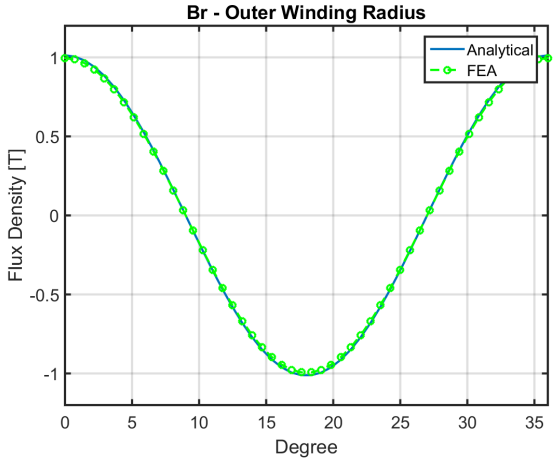

(c) Outer Winding Radius

Figure 3.3: Radial Flux Density Comparisons with FEA

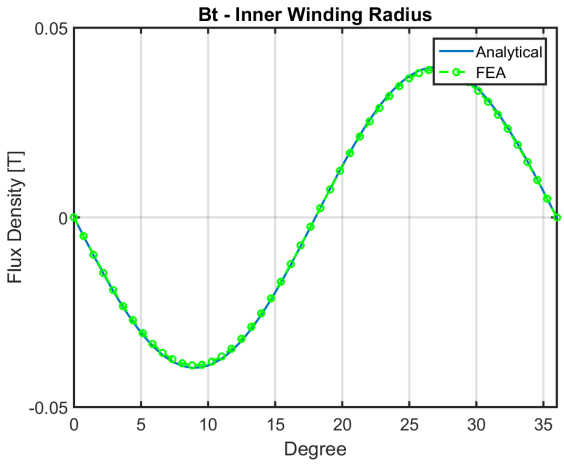

(a) Inner Winding Radius

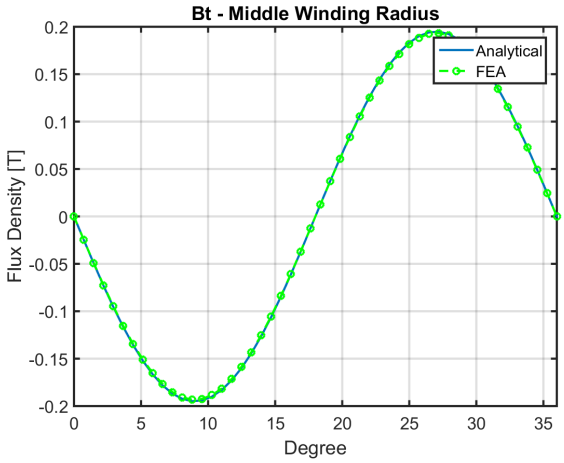

(b) Middle Winding Radius

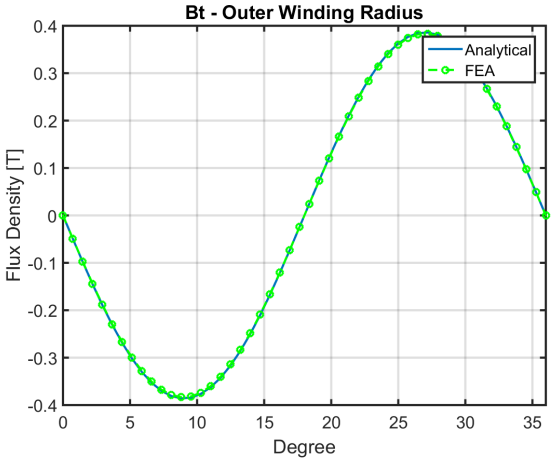

(c) Outer Winding Radius

Figure 3.4: Tangential Flux Density Comparisons with FEA

Table 3.2: Odd Harmonics of Radial Flux Density at Outer Winding Radius

Harmonic Number	Normalized Amplitude
1	99.50%
3	0.03%
5	0.03%
7	0.02%
9	0.02%
11	0.08%
13	0.36%
15	0.08%

Table 3.3: Average Torque Prediction Comparison with FEA

Speed	18000	RPM
Pole pair	10	
Slot Current Density	8.38	$Arms/mm^2$
FEA Average Torque	512	Nm
Analytical Average Torque	540	Nm
Error	5.47%	

Figures 3.3–3.4. The flux distribution at three different radius positions in the winding region has prediction error of around 2% compared to the FEA. However, the developed EM analytical solutions do not predict flux harmonics or account for segmented geometry effects in the Halbach PM array. A more general analytical solution of the segmented Halbach PM array will be derived in the future research. At this stage, it is sufficient to come up with an initial sizing of the proposed motor topology with the developed EM modeling.

The 13th harmonic has slightly larger magnitude of 0.36 % compared with the fundamental one shown in Table 3.2. This is because 12 segments of the PM array are used to form one complete pole pair. In other words, there are 13 segment gaps due to imperfect contact among magnet segments. If the segment number for each pole pair increases, harmonic effects can be reduced further and the magnetic flux waveform will be closer to a perfect sinusoidal waveform. Undesired harmonics can induce large torque ripples, which enhance undesired motor vibrations and more copper losses, which result from eddy-current-loss in time-varying magnetic flux.

Since the average torque is primarily determined by the fundamental radial

flux density, only the fundamental waveforms are compared in this case. And the flux density produced by the Halbach array is the closely sinusoidal waveform according to harmonic analysis shown in Table 3.2. The average torque estimation error is around 5% compared with the FEA result shown in Table 3.3. The errors in the magnetic flux density estimation propagate to the torque prediction, so the torque estimation errors could result from the assumptions made before.

CHAPTER 4

HEAT LOADS ESTIMATION

Heat loads might seem a trivial task at first sight, since the resistance of a wire with known length and uniform cross section can be calculated using simple circuit theory. The truth, however, is that the physical phoneme is complex. The computation of losses can be one of most difficult and challenging aspects of machine design. Not all physical processes can be easily described by well-established theories. Some of them are currently not understood, although new computational and theoretical techniques come out. For example, there exists no general analytical solution to the famous fluid dynamics governing equations—the Navier-Stokes equations—which describe the motion of viscous fluids. Thus, mechanical losses, such as viscous friction losses, in machine design, are extremely difficult to compute and quantify theoretically. This chapter focuses on using established methods to predict heat loads, including copper loss, iron loss, and mechanical loss, for the following thermal analysis and temperature prediction. Some reasonable assumptions are made to simplify the problems and fit into established methods.

4.1 Copper Loss

Copper loss is a significant heat source in this motor design, accounting for roughly 30% to 60% of total losses. Since windings are in the main path of magnetic flux, eddy current effects could boost copper loss while pure copper current density is not large at all. In order to resolve the negative influences of induced current losses in the windings, Litz wire is utilized to minimize eddy current effects. Basically, instead of using a bulk of copper to conduct electric loading, a large number of strands with much smaller diameters are bundled together and radially transposed to minimize AC loss. Although conduction losses in windings are easy to calculate, the problem is complicated by the

fact that the current distribution in conductors is not always uniform.

4.1.1 DC Loss

DC loss is generally equivalent to ohmic loss in conductors due to the conduction friction property of metal under electric field. Assume uniform current density on the cross section of conductors. Given pure copper volume of windings and copper current density, DC loss can be estimated by

$$P_{dc} = J_{cu\_rms}^2 V_{cu} \rho_{cu} \tag{4.1}$$

Additionally, copper resistance can be affected by operating temperature. For copper wires, every 100 degree rise in temperature results in approximately 40% increase in conductor resistance. To precisely predict copper loss, thermal effects have to be accounted for. The relation of copper resistivity to temperature is given as

$$\rho_{cu}(T) = \rho_{cu\_0} \left[1 + \alpha_{cu}(T - T_0)\right] \tag{4.2}$$

where reference copper resistivity at 20 °C, ρ_{cu_0}, is 1.68×10^{-8} Ω·m and copper temperature coefficient α_{cu} is 3.862×10^{-3} K^{-1}.

4.1.2 AC Loss

AC loss in conductors is mainly composed of skin effect and proximity effect due to induced eddy current in time-varying or space-varying magnetic field. In this motor, Litz wire is utilized to minimize AC loss by (1) eliminating skin effects by using small strands, and (2) reducing proximity effects by insulating multi-strand conductor bundles.

Originally, the method developed by [10] was intended for analyzing AC loss not in Litz wire, but in low-cost multi-stranded wire. In order to adapt it to this motor design, several assumptions need to be made. According to the configuration of Litz wire provided by New England Wire Company, interstrand resistivity (ρ_{ss}) is close to infinity, since multi-strand bundles are wrapped with specific insulation to reduce eddy current loop size in conductors. Also, each strand is coated with insulator to decrease induced current

loss further. Accordingly, interstrand resistivity can be set to one for this type of Litz wire.

Furthermore, the formulas developed by [10] only consider single excitation frequency effects. Nevertheless, the magnetic field in the machine winding and gap regions is not perfectly sinusoidal, involving harmonics due to magnetic traveling waveform distortion. One solution is to adopt frequency analysis, such as FFT, to find out the magnetic flux magnitude at different harmonic frequencies and associated induced current losses. Since harmonic effects of such machine topology are negligible according to Table 3.3 on page 20, it is reasonable to assume that windings can only see fundamental sinusoidal external magnetic field, which perfectly fits into the applicable range of the model developed by [10].

Pitch is a key determinant parameter in Litz wire configuration. It describes how strands twisted around the bundle center can affect eddy current loss. Due to transposed technique used in Litz wire configuration, conductor current distribution and effective conductor length can be rather different from normal wires. Optimal pitch (p_{opt}) is a good approximation in AC loss prediction, if detailed pitch dimension is not available. Optimal pitch can be computed by

$$p_{opt} = \sqrt[4]{\frac{\pi^4 \rho_{ss} n d_s^4}{16\rho_{cu}} + \frac{32 I_{rms}^2 \rho_{ss} \pi^2 \rho_{cu}}{\omega_0^2}} \tag{4.3}$$

where n is the total strand number in Litz wire, d_s is strand diameter, ρ_{cu} is copper resistivity, I_{rms} is the rms current fed into Litz wire, and ω_0 is fundamental excitation frequency.

Obtaining magnetic field distribution at each point in the machine is challenging because of the complexity of analyzing Maxwell's equations. With the EM model developed in Chapter 3, an analytical solution of average square magnetic field ($\overline{B_{pk}^2}$) in the winding region required for AC loss prediction can be derived from Equations 3.22 to 3.24 shown as

$$\overline{B_{pk}^2} = \frac{2(1+\mu_r)^2}{R_w^2 - R_{sy}^2} \left\{ \frac{4B_{rem}}{D_0} \frac{p}{1-p} \left[1 - \left(\frac{R_r}{R_m} \right)^{p-1} \right] \right\}^2 \left\{ \frac{R_w^{2p} - R_{sy}^{4p} R_w^{2p}}{2pR_r^{2p-2}} + \frac{2R_{sy}^{2p}(ln(R_w/R_{sy}))}{R_r^{2p-2}} \right\} \tag{4.4}$$

The key component $\overline{B_{pk}^2}$ in AC loss prediction is verified with FEA result.

38 AWG Litz wire with 0.244" (width) by 0.215" (height) is selected for this motor design. The slot area is fixed at depth 0.215", which is composed of 3 turns. Analytical prediction of $\overline{B_{pk}^2}$ is 0.998 T^2, which has an error of roughly 2.5% compared with the FEM result 0.973 T^2. It indicates that the developed equation has a good agreement with the FEM method.

Due to small skin depth effects and insulated bundle/strand configuration, AC loss in the conductor is dominated by the strand eddy-current loss. With given average flux density in the winding region and optimal pitch dimension, and other known parameters, eddy-current loss in strand level is given as [10]:

$$P_{strand} = \frac{\pi\omega\overline{B_{pk}^2}d_s^2 nl}{128\rho_c u}\left(1 + \frac{\pi^2 n d_s^2}{4K_{cu}p_{opt}^2}\overline{B_{pk}^2}nd_s^2\right) \tag{4.5}$$

where K_{cu} is Litz wire fill factor.

4.2 Iron Loss

Iron loss is also another challenging part of prediction. Currently, there is no rigorous theory that can describe the iron loss dynamic accurately. Empirical relation is often used and coefficients can be extracted by curve fitting of experimental results. Beyond traditional hysteresis and eddy loss based on physical justifications, a statistical loss theory adds anomalous loss to account for excess contributions arising from random magnetic distribution and dynamic effects. According to this theory, iron loss with sinusoidal excitation can be estimated as [11]:

$$P_{iron} = P_h + P_e + P_a = k_h f B^2 + k_e f^2 B^2 + k_a f^{1.5} B^{1.5} \tag{4.6}$$

where k_h is the hysteresis loss coefficient, k_e is the eddy current loss coefficient, and k_a is the anomalous loss coefficient. This formula is not sufficiently general and some deviations might be observed, since coefficients can depend on flux density and electrical frequency.

4.3 Windage Loss

Windage loss in an electrical machine is the power absorbed by the fluid around the rotor as a result of relative motion between the spinning rotor and ambient fluid. Since the power absorbed by the surrounding does no work to move the shaft, windage loss hurts electrical machine overall efficiency and even mechanical torque. Another undesirable characteristic of windage loss, which is even more important, is that the loss is converted into heat which raises the temperature of the rotor and stator where friction occurs. Therefore, it is crucial to predict the windage loss of the proposed motor design to assess its feasibility in terms of both efficiency and heat.

Quantifying friction and windage losses can be even more difficult than eddy-current loss prediction. Since a self-pumped air cooling scheme is picked and rotating speed is quite high, fluid dynamics could become unpredictable and full of uncertainties. At the current stage, no literature reports a study of rotating cylinder or concentric rotating cylinders rotating at such high tip speed in the air. Developed fluid dynamics theories might not be able to cover this type of rotating fluid problem. Also, gap thickness is extremely small compared with other machines. Both experiments and fluid dynamic modeling have difficulty measuring and predicting the flow behavior for such a case.

Two main components generate tremendous windage and friction loss. One is the outer surface of the rotating rotor. The other is the gap between the concentric cylinders while the outer cylinder is rotating. Disk windage loss could become non-negligible in some cases. All these windage losses result from turbulent flow during high-speed rotor spinning.

Quantifying turbulent flow is quite difficult because flow is so unstable. Computational fluid dynamics (CFD) is one way to resolve this problem; however, it does not always predict well all the time. And prediction uncertainties, modeling difficulty, and computation capability limitations add more obstacles to CFD method. Empirical correlation is an easier way to estimate windage loss. Similar problems exist in utilizing empirical methods, such as result uncertainty and geometry differences.

Several assumptions are made for approximations to simplify the problems:

1. Rotating cylinder and disk have perfectly smooth surfaces.

2. Tangential flow is dominant and thus axial flow effects are ignored.

3. The correlations are regarded as valid, though the Reynolds number in the baseline design is beyond valid range.

4. Air physical properties are uniform across the whole computation space.

5. No thermal effects are considered at this estimation stage

4.3.1 Outer Rotor Windage Loss

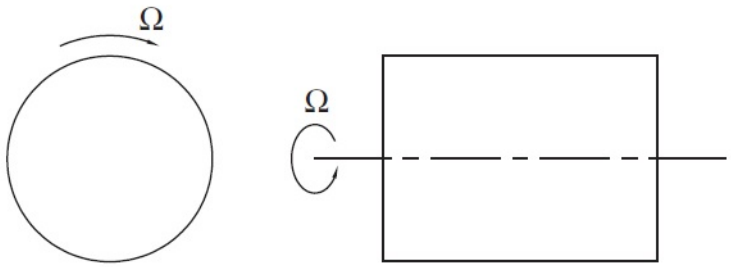

Figure 4.1: Rotating Cylinder Configuration [12]

One important part of windage loss is generated outside the high-speed rotating rotor shown in Figure 4.1. Air is assumed to be initially stationary and other walls might exist in the space where the motor spins. High-speed rotation of the rotor can cause surrounding air to move around. Turbulent flow forms in this case due to high rotating movement, and a huge amount of turbulent eddies occur causing heat and friction among air particles.

An empirical correlation is used for initial approximation of windage loss generated at the outer surface of the rotor during rotating. The problem is simplified as a rotating cylinder in free stream.

The Reynolds number of a rotating cylinder in free stream is defined as

$$Re = \frac{\omega_m R^2}{\nu} \tag{4.7}$$

where ω_m is the cylinder rotating speed, R is rotating cylinder outer radius, and ν is dynamic viscous coefficient. The friction coefficient (C_{mc}) empirical

relation is given as [12]:

$$C_{mc} = \left(\frac{1}{-0.8572 + 1.25ln(Re\sqrt{C_{mc}})} \right) \tag{4.8}$$

With the calculated friction coefficient, the windage power outside the rotor is

$$P_{wind\_outer} = \pi C_{mc} \rho R_o^4 \omega^3 L \tag{4.9}$$

where L is axial length of the rotating cylinder. One thing to note here is that the selected empirical relation valid range does not fit into the proposed motor condition. Estimation results have large uncertainties.

4.3.2 Gap Windage Loss

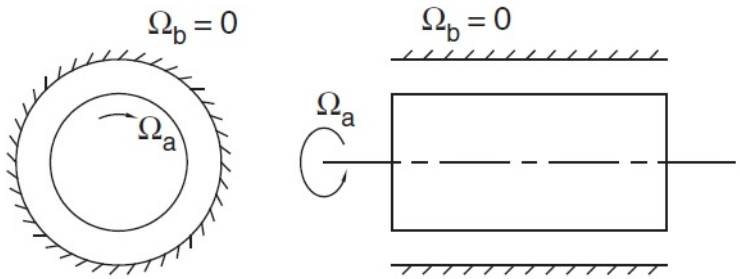

Figure 4.2: Annulus with Inner Cylinder Rotating Configuration [12]

Another important portion of windage loss occurs in the gap between rotor and stator. While the rotor spins, air particles in the gap move at high speed and interact with stator surface closely due to extremely small gap thickness. The stator surface and air itself have viscosity which adds friction to particle movements. The windage loss in the gap between rotor and stator shown in Figure 4.2 is simplified as concentric cylinders with the outer cylinder rotating.

Most studies have addressed the case where the inner cylinder rotates while the outer is the stator, which is opposite to this design. The assumption is made that the outer cylinder rotation of concentric cylinders is similar to inner cylinder rotation. So empirical correlations that work for inner cylinder rotation are still valid here.

The Reynolds number for rotating concentric cylinders is different from that for cylinder rotation in the free stream. It is defined as

$$Re = \frac{\omega_m R\delta}{\nu} \tag{4.10}$$

where ω_m is the rotating speed of the inner cylinder, R is the inner rotating cylinder outer radius, and δ is the gap between the concentric rotating cylinders.

The empirical correlation is selected from Vrancik [13], given as

$$\frac{1}{\sqrt{C_d}} = 2.04 + 1.768ln(Re\sqrt{C_d}) \tag{4.11}$$

where C_d is the friction coefficient for this condition. Gap windage loss (P_{wind_gap}) can be calculated in a similar way as

$$P_{wind\_gap} = \pi C_d \rho R_r^4 \omega^3 L \tag{4.12}$$

Similar problems exist in this approximation. Since the extremely small gap ratio of the proposed motor has never been studied experimentally, developed empirical correlations might result in a large range of uncertainties and errors. Nevertheless, at the initial sizing study stage, it is beneficial to have a rough approximation of windage loss to eliminate infeasibility of design.

4.3.3 Rotating Disk Windage Loss

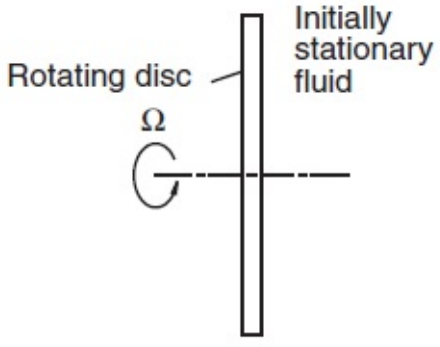

Figure 4.3: Rotating Disk in Initially Stationary Fluid Configuration [12]

Other than windage losses generated on the outer and inner surfaces of the rotor, the rotor ending surface also generates heat while overcoming friction from rotating in the air, shown in Figure 4.3. When the rotor outer radius increases, disk windage loss becomes nonnegligible. To quantify this, [14] studied this fluid dynamics case experimentally and developed a correlation of friction coefficient and Reynolds number.

The Reynolds number is defined as in the rotating cylinder in free stream case. The empirical correlation of the friction coefficient in a rotating disk in free stream is given as [14]:

$$C_m = 0.491[log_{10}(Re)]^{-2.58} \quad (10^4 \leq Re \leq 10^9) \tag{4.13}$$

Windage loss associated with the rotating disk is defined as

$$P_{wind\_disk} = 0.5\rho\omega^3 R^5 C_m \tag{4.14}$$

This correlation is not perfectly accurate for predicting friction loss generated by a rotating disk. However, it has far less uncertainty than predicting the windage loss of rotating cylinders, since so many studies have been carried out and they converge to similar results.

CHAPTER 5

WINDING EQUIVALENT THERMAL CONDUCTIVITY PREDICTION

Winding, one of the most important components in an electrical machine, carries current to generate torque. More than half of machine loss results from copper losses generated in windings. Also, inherent machine configuration does not allow coolant to access windings easily. Usually, heat from the copper needs to be conducted through many layers of different materials and then be removed by coolant. Therefore, the hotspot temperature of an electrical machine most likely occurs at the winding region.

One of the difficulties in thermal analysis is to accurately model winding equivalent thermal conductivity. Complete solid copper is rarely used in windings due to high induced current loss, especially at high frequency operation. Insulation has to be embedded within different turns, bundles or even strands to separate different turns and layers, reduce eddy-current loss and avoid short-circuit. If the winding consists of many wires and insulation layers, such as Litz wire, it is difficult to model them specifically in the analysis. A simplified equivalent thermal model of the winding has to be employed to predict machine performance more quickly.

Instead of capturing all small component geometries and physical properties in the winding modeling, homogenization techniques can be applied to find substitutes with equivalent physical properties and performance, which is a key enabling factor in accurate and efficient thermal modeling and analysis. In this chapter, a simplified analytical method and simulation method to quantify equivalent thermal conductivity of windings are discussed in detail. Other than homogenization techniques, corresponding bench test set-up and results are presented and compared.

5.1 Winding and Litz Wire Configuration

In high frequency machines, AC losses due to eddy-current induced in the copper windings significantly restrain the allowable electrical loading. One winding technique, often used in high-frequency transformers, is Litz wire. Litz wire consists of many individually insulated small strands separated into several bundles that are radially transposed. Small insulated individual strands and bundles can decrease skin and proximity effects by breaking down the induced-current loop in conductors. Transposition techniques can distribute induced current more uniformly in conductors by rotating strand space positions.

Each coil consists of three turns of Litz wire within the slot space. The staggered winding configuration illustrated in Figure 5.1 was selected for its lesser end-winding replicability. Different phases can be assembled together with different ending axial length without interfering with each other. The Litz wire used in this proposed motor consists of 660 AWG 38 strands separated into 15 bundles as shown in Figure 5.1. Each strand surface is brushed with a heavy coating. Forty-four strands form a bundle wrapped with Nylon insulation, which has the lowest material temperature limit in the whole machine. Other specifications of the selected Litz wire are presented in Table 5.1. Different types of insulation—RTV and resin—are employed to firmly bundle Litz wires in specifically designed slot geometries. Also, resin is expected to fill air voids within windings to improve thermal conductivity. The thermal properties of different winding materials are listed in Table 5.2.

Table 5.1: Litz Wire Key Metrics

Height	0.063	inch
Width	0.244	inch
Bundle Number	15	
Strand Number	44	
Copper Fill Factor	52.5%	

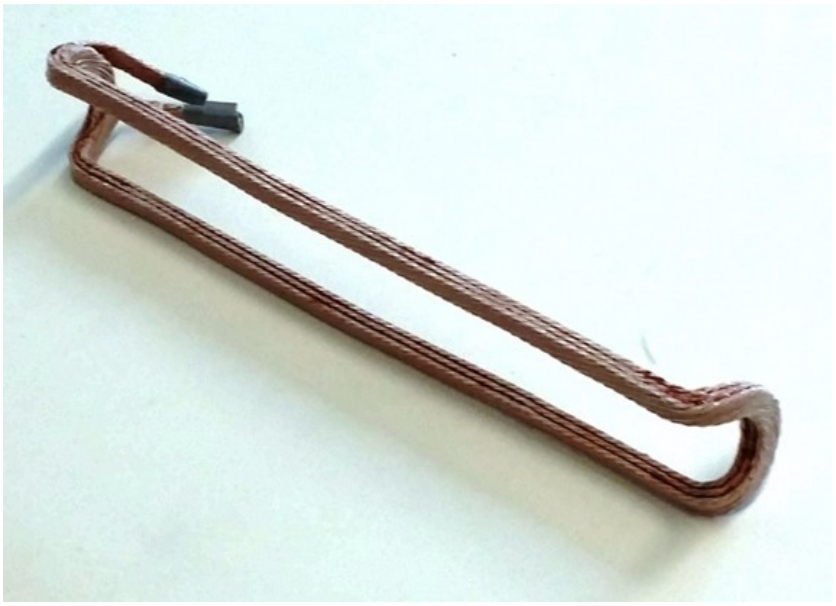

(a)

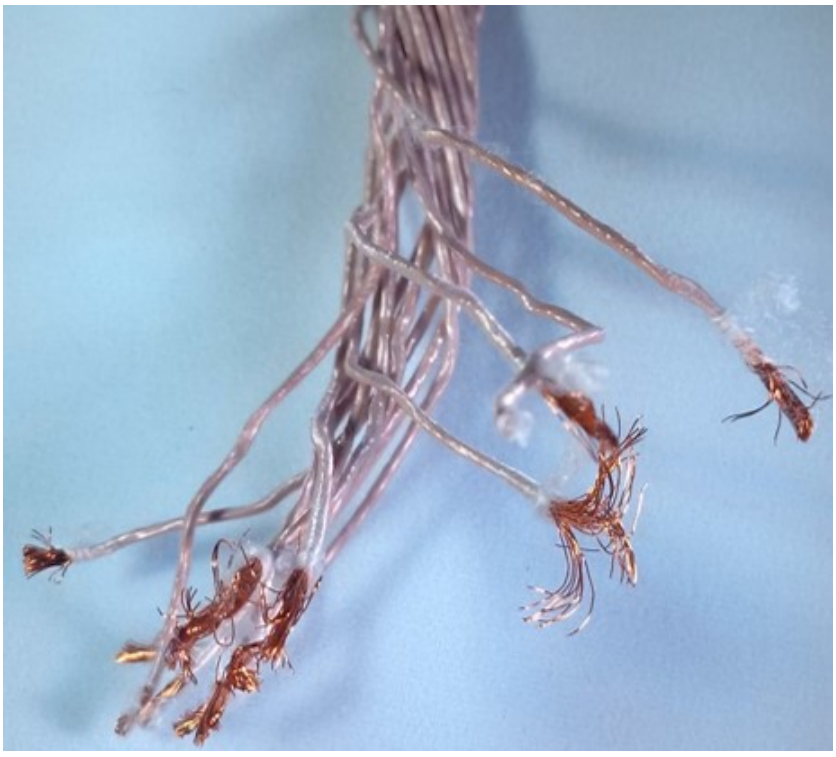

(b)

Figure 5.1: (a) Staggered Winding Made by Litz Wire, (b) Litz Wire Strands Separated as Bundles

Table 5.2: Thermal Properties of Winding Materials

	Type	Thickness	Max Temp	Thermal Conductivity
Strand	Polyimide Film (MW 16-C)	1	240	0.1
Bundle	Nylon	3	155	0.25
RTV	RTV 108		204	0.207
Resin	Devcon Ceramic Red		176	0.804

5.2 Equivalent Thermal Conductivity of Slotless Windings

One composite homogenization technique is to use a simplified analytical model. An arbitrary winding slot is shown in Figure 5.2. An equivalent rectangular copper area substitutes for a uniformly distributed small strand copper area. Similarly, the area equivalent principle is also applied to replace the distributed insulation region and epoxy resin. One big missing part in this equivalence modeling is bundle insulation. Also, detailed strand positions cannot be accounted for in this case. Air voids are assumed to be perfectly filled with epoxy resin. In the initial sizing process, this technique can be applied.

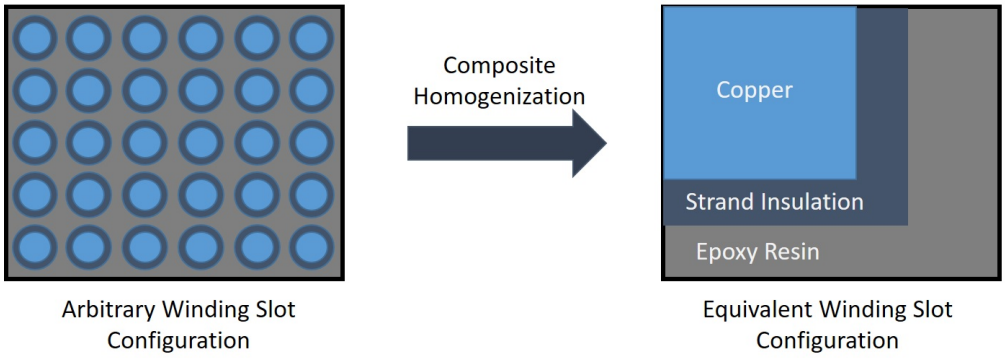

Figure 5.2: Composite Homogenization in Arbitrary Winding Slot and Wires

With given copper fill factor, strand size, strand insulation thickness, and wire dimensions, equivalent radial thermal conductivity can derived as fol-

lows:

$$k_{eq\_radial} = \frac{1}{R_1} + \frac{1}{R_2} + \frac{1}{R_3} \tag{5.1}$$

$$\frac{1}{R_1} = \frac{\sqrt{ff}}{\frac{\sqrt{ff}}{k_{cu}} + \frac{\frac{t_{ins}}{r_{cu}} \cdot \sqrt{ff}}{k_{ins}} + \frac{(1 - \sqrt{ff} - \frac{t_{ins}}{r_{cu}} \cdot \sqrt{ff})}{k_{res}}} \tag{5.2}$$

$$\frac{1}{R_2} = \frac{\frac{t_{ins}}{r_{cu}} \cdot \sqrt{ff}}{\frac{(1 + \frac{t_{ins}}{r_{cu}}) \cdot \sqrt{ff}}{k_{ins}} + \frac{(1 - \sqrt{ff} - \frac{t_{ins}}{r_{cu}} \cdot \sqrt{ff})}{k_{res}}} \tag{5.3}$$

$$\frac{1}{R_3} = (1 - \sqrt{ff} - \frac{t_{ins}}{r_{cu}} \cdot \sqrt{ff}) \cdot k_{res} \tag{5.4}$$

where ff is copper fill factor, t_{ins} is strand insulation thickness, r_{cu} is strand radius, k_{cu} is copper thermal conductivity, k_{ins} is strand insulation thermal conductivity, and k_{res} is epoxy resin thermal conductivity.

For a similar equivalent technique, axial thermal conductivity of Litz wire can be approximated with the derived equation as

$$k_{eq\_axial} = k_{cu}\frac{A_{cu}}{A_{wire}} + k_{ins}\frac{A_{ins}}{A_{wire}} + k_{resin}\frac{A_{resin}}{A_{wire}} \tag{5.5}$$

where A_{cu} is total copper area, A_{wire} is wire cross section area, A_{ins} is total insulation area, and A_{resin} is total epoxy resin region area in the Litz wire.

Table 5.3: Slot Key Metrics

Height	0.215	inch
Width	0.254	inch
Turn Number	3	

Another composite homogenization technique is to simulate performance with exact geometry specifications. As presented in Figure 5.3, Litz wire can be modeled exactly as specified in Table 5.3. A thermal test scenario can be artificially created in the 2D FEA software, Flux2D. The core idea is to force heat to flow radially to simplify the problem as one-dimensional. A fixed high temperature is assigned at the top winding boundary. The bottom of the wire is assigned an arbitrary convection boundary condition. In this case, the heat transfer coefficient (h_{conv}) is set at 100 W/mK and the coolant ambient temperature (T_a) is 20 °C.

Thermal steady state analysis is conducted to predict the temperature dis-

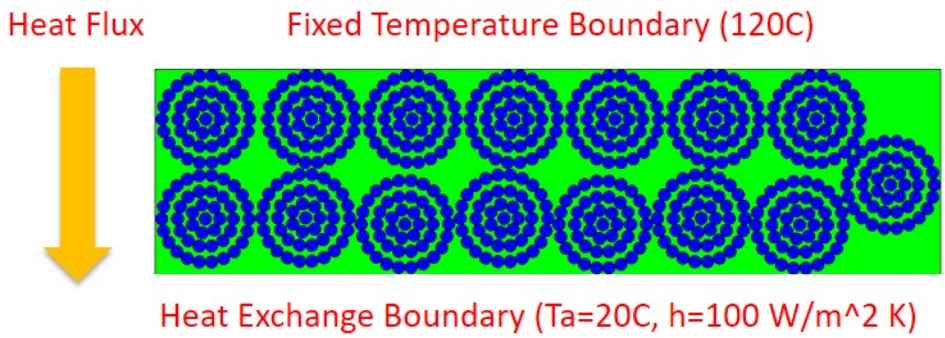

Figure 5.3: Simulation Prediction Method of Armature Equivalent Radial Thermal Conductivity

tribution in the winding. The wire bottom temperature is taken to calculate the equivalent radial thermal conductivity (k_{eq_radial}) of Litz wire by using a derived equation:

$$h_{conv}(T_{bottom} - T_a) = k_{eq\_radial}\frac{T_{top} - T_{bottom}}{H_{wire}} \tag{5.6}$$

where T_{top} is the measured temperature at the top of the winding, T_{bottom} is the measured temperature at the bottom side, and H_{wire} is the wire cross section.

5.3 Experimental Verification

5.3.1 Bench Test Set-up

One concern is voids in the armature winding. If epoxy resin does not penetrate the winding cross section and fill all the voids in the windings, air voids can harm effective radial equivalent thermal conductivity dramatically and induce unexpected hotspots during operation. The thermal simulation does not capture the air voids in the armature winding. Also, the contact resistance is not considered in the thermal simulation when predicting the effective thermal conductivity.

In order to verify the equivalent radial thermal conductivity of the armature winding, a bench test is set up to measure the equivalent thermal conductivity in the winding. Basically, a scenario is created to force the

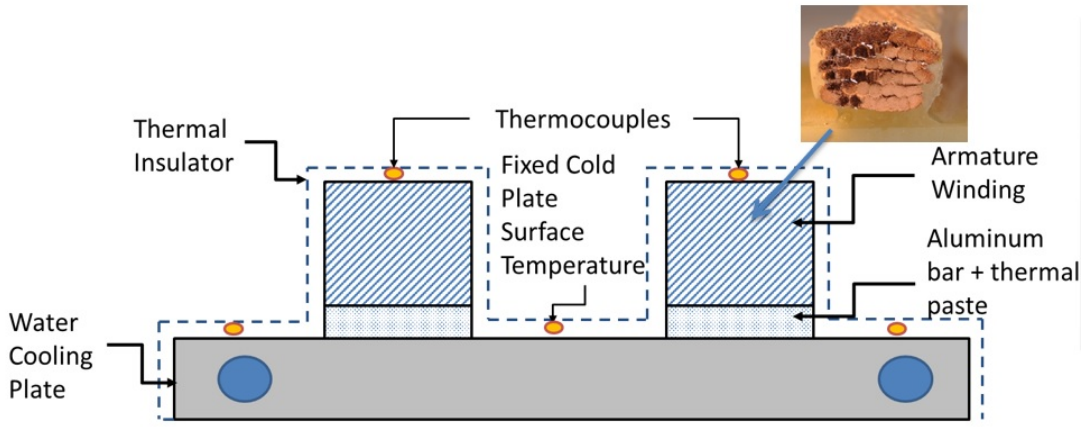

Figure 5.4: Armature Winding Effective Radial Thermal Conductivity Verification Bench Test

heat to flow radially. The winding is surrounded with insulator foam on all sides except the bottom, which is attached to the cold plate. Between the bottom of the winding and the cold plate, an aluminum bar is inserted for better contact and heat conduction to the cold plate. The cold plate contains the water cooling pipes and is connected to the outside water cycling system. The cold plate fixes the bottom temperature of the coil. Thermal compounds are also applied at the different contacting surfaces to reduce the thermal contact resistance effects.

The specific set-up illustration is shown in Figure 5.4. There are 8 thermocouples embedded in the set-up. Three thermocouples are attached to each bar of the coil at the middle and two other ending locations. The other two thermocouples are inserted between the aluminum bar and cold plate. The highest temperatures are expected at the top of the winding coil due to the insulator wrapped around it allowing no heat flux directly to the outside except towards the cold plate. Ideally, the temperature on the cold plate is expected to be uniform, but there could be unconsidered factors that cause it to vary over the plate.

The coil is embedded inside the pink insulator block shown in Figure 5.5. The end of the coil might extend slightly outside the insulator block, but it is also wrapped by the thermal insulator paper. Sealing of the coil ends might be imperfect and cause heat to leak to the ambient air. The aluminum bars are put on the bottom side of two bars of coil and coated with white thermal compound. In the end, the cold plate is attached to the aluminum surface

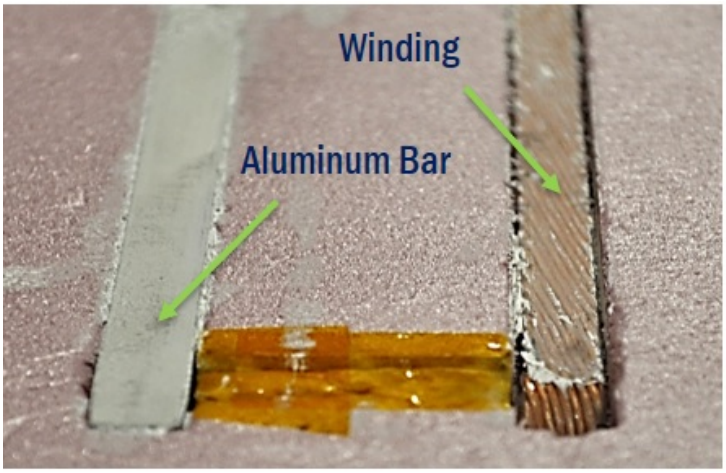

(a)

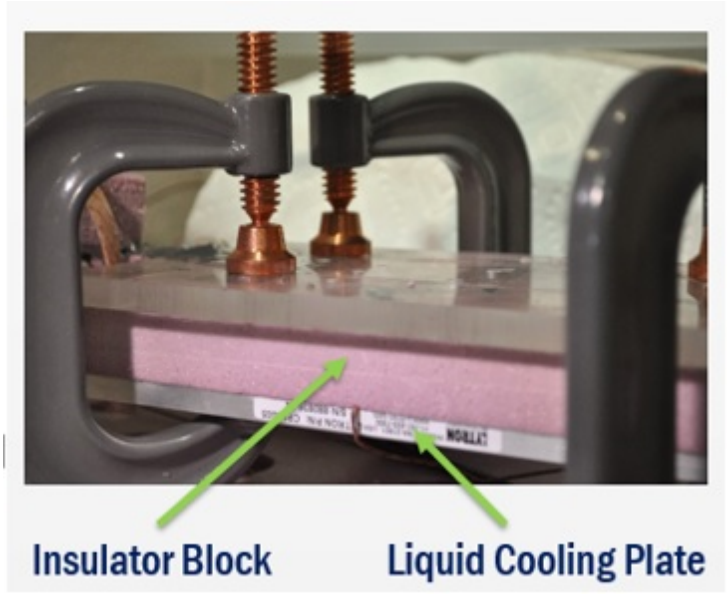

(b)

(c)

Figure 5.5: Winding Equivalent Radial Thermal Conductivity Bench Test

with clamps. Even with the higher pressure at which cold plate and insulator block are clamped, air gaps cannot be completely eliminated between them due to imperfectly smooth contacting surfaces.

The temperature difference due to copper loss was calculated according to measured hotspot temperatures on the top of the winding and measured temperatures on the cold plate surface. Average measured temperature values at two different locations were used to estimate the radial temperature gradient across the winding coil. The equation to quantify the radial temperature gradient across the winding yields

$$\triangle T_{rise} = AVG(T_{hotspot}) - AVG(T_{coldplate}) \tag{5.7}$$

where $AVG()$ is an average function.

5.3.2 Simulation Set-up

Prediction of the equivalent radial thermal conductivity of the coil is implemented numerically in Flux 2D FEA software. The equivalent radial thermal conductivity of selected Litz wire can be estimated according to Equation 5.6, which is around 0.49 W/mK. The set-up of FEA boundary conditions is exactly the same as in the bench test. The insulator boundary conditions are applied on all sides of the coil except the bottom. The bottom of the simulation set-up is assigned a fixed temperature boundary condition according to the measured average cold plate temperature.

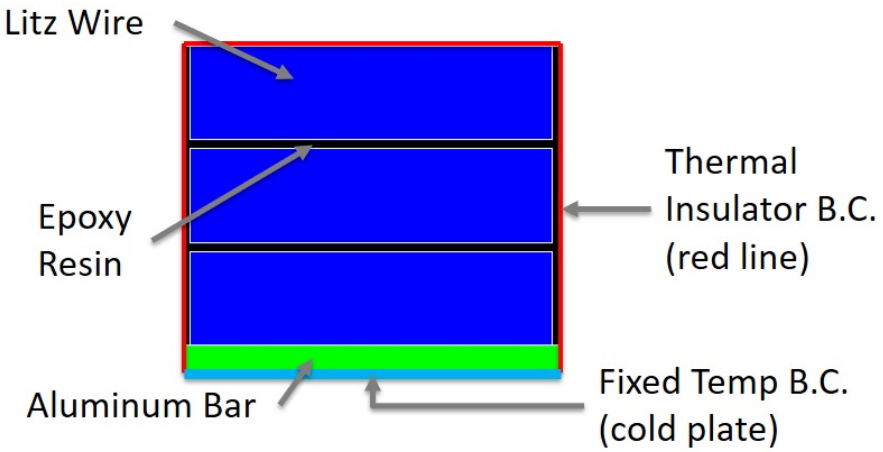

Figure 5.6: Equivalent Simulation Set-up

Figure 5.6 illustrates the detailed cross section of the coil attached to an aluminum bar and cold plate. The blue portion in Figure 5.6 is the coil filled with silicon resin. The black region is the applied epoxy resin. The green region is the aluminum. The bottom side is the fixed temperature boundary condition, because of the large heat capacity of the cold plate filled with cycling cool water.

The heat source can be estimated according to various feed-in dc currents during the test. Other boundary conditions, dimensions, and physical-thermal conductivities of components in the bench test set-up are exactly the same as in the simulation modeling. If winding radial thermal conductivity is predicted correctly, the temperature rise of hotspot locations in the simulation will match the experimental measured temperature rise.

5.3.3 Result Comparisons and Discussion

The coil is fed with different dc currents and corresponding hotspot temperatures on the coil and cold plate are recorded. The measured resistance of the coil is around 8 mΩ, which might be slightly greater than the real case due to incomplete removal of insulation on the coil connections. The maximum current allowed without hitting the insulator material temperature limit is 68 A. However, the expected rated coil phase current is over 70 A.

Figure 5.7 (a) shows the sample experimental data of average hotspot temperatures on the coil during the whole monitoring period. During the four hour test, the hotspot temperature reached steady state indicated by the flat slope, at the end. The noise in the measurement curve might result from the power supply and water cycling system.

Figure 5.7 (b) summarizes the theoretical and experimental hotspot temperature rises varying with input dc current of the power supply. The theoretical prediction values are slightly lower than experimental values because equivalent thermal conductivity might be underestimated and there is heat flux leakage in the set-up. The maximum current used in the test is lower than the rated current in the baseline machine design due to temperature limitations of the insulator block.

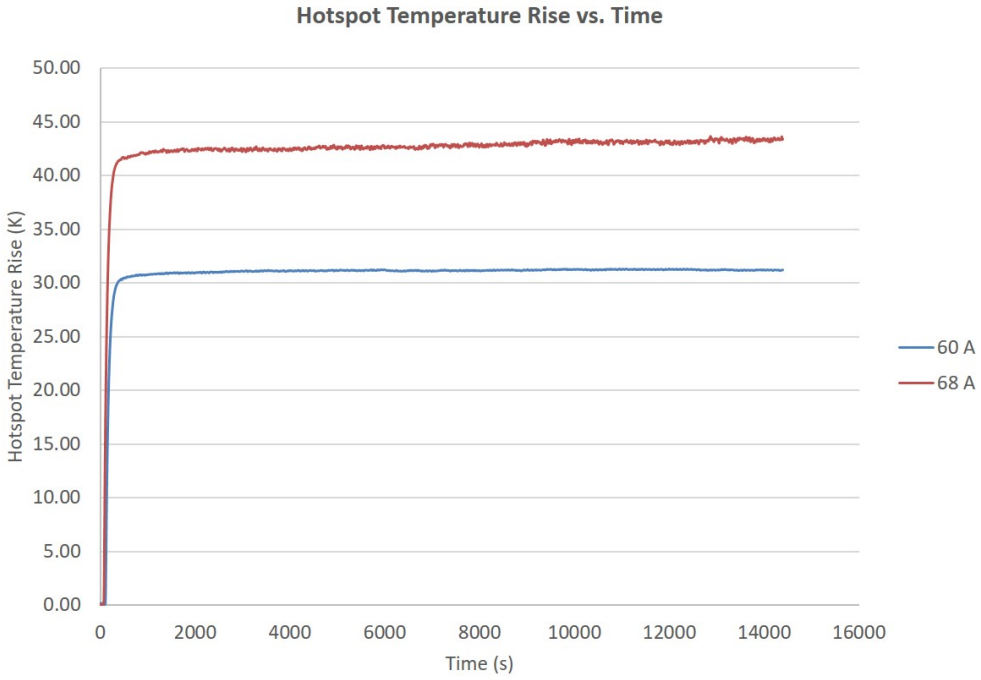

(a)

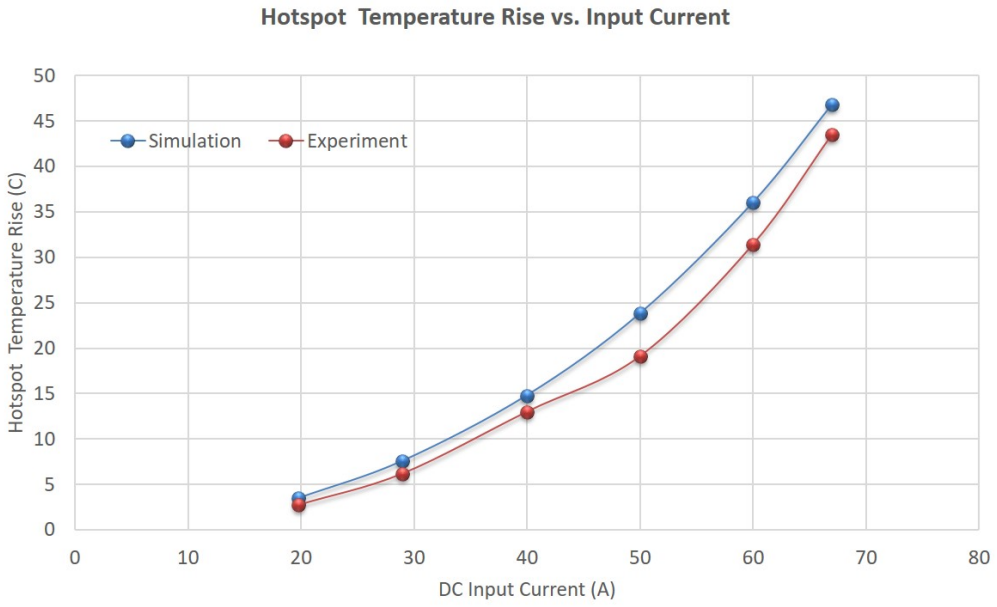

(b)

Figure 5.7: Winding Thermal Bench Test Results: (a) Average Hotspot Temperature vs. Time when Phase Current = 68 A and 70 A; (b) Comparisons Between Simulation and Experimental Hotspot Temperature Varying Current

CHAPTER 6

THERMAL ANALYSIS

Conventional industrial electrical machine design focuses on electromagnetic analysis with assumed electric loading based on experience or rules of thumb. Nevertheless, meeting high-power-density machine design challenges requires pushing magnetic loading, electric loading and rotating speed as high as possible. Instead of separating thermal analysis from EM analysis, as in traditional machine design, conducting multi-physics optimization of machine sizing can boost machine power density by taking advantage of the coupling of electromagnetic and thermal physical parameters. Detailed thermal analysis is one of the key steps in multi-physics optimization modeling.

This chapter first introduces the cooling scheme used in this proposed motor design. With the specified cooling scheme, detailed cooling capability can be estimated with empirical relations and reasonable assumptions. Then, a simplified thermal analysis model is derived to predict motor hotspot temperature efficiently and accurately.

6.1 Overview of Thermal Management

An aggressive self-pumped air cooling was picked to remove heat loss and cool the motor within temperature constraints simultaneously. Electric loading of the baseline motor design accords with liquid cooling according to past rules of thumb. Despite the fact that liquid cooling is the most effective cooling method, it is impossible to employ liquid cooling at this stage because of the critical weight constraint and the complexity of adding a pump system for extra coolant. Aggressive forced-air cooling is the only feasible thermal management method to pursue in this motor design.

Three important thermal challenges in high-power-density motor design need to be addressed. The first one is to generate sufficient coolant to remove

heat effectively, which mainly relies on a fan design to pump enough cooling air through the motor. In this proposed motor, centrifugal fan topology was selected due to its small volume, effective pumping capability and low pressure. The current fan blade, which is mounted on the inner surface of the rotor disk, is shown in Figure 6.1. When the rotor spins, centrifugal fan attracts cooling air from the back of the motor through cooling channels and gap, and releases warm air through outlet holes at the outer rotor surface. The challenges in fan design are strict space constraint and complicated fluid dynamic analysis. Strict space constraint results from critical rotor shape. It is very unlikely to adjust rotor geometry to adopt bigger fan blades because of critical rotor integrity and vibration during high-speed operation. Small changes in rotor geometry require a great many mechanical considerations.

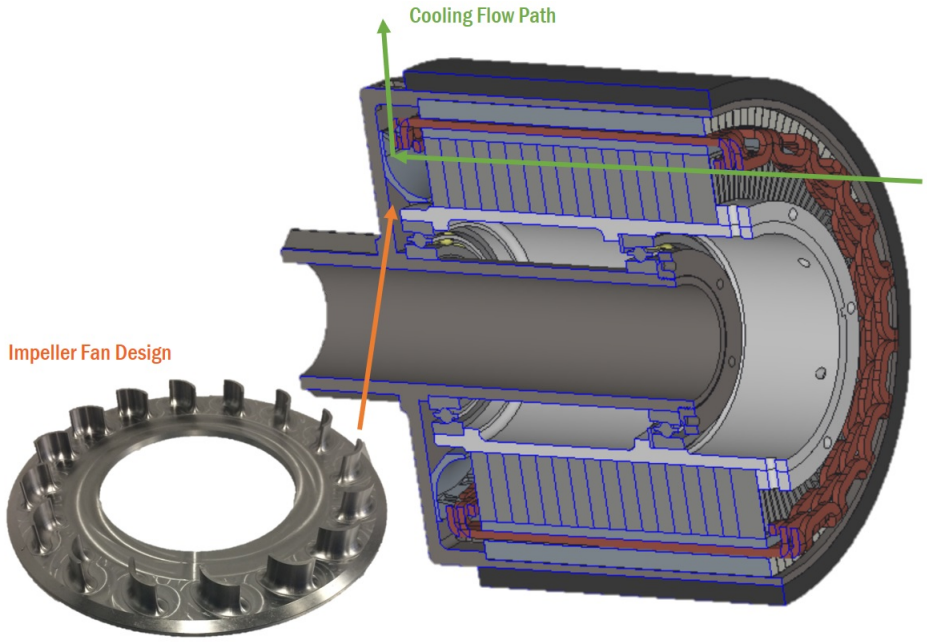

Figure 6.1: Initial Centrifugal Fan Design

The second challenge in thermal management is how to conduct heat effectively towards a cooling surface. Due to motor topology, the winding region has to be mounted far away from the heat sink. Even though a power fan can pump adequate cooling flow through the heat sink, if thermal resistances in the heat conduction path are too large, a huge temperature gradient can be created. In other words, the hotspot temperature cannot be lowered despite sufficient cooling flow provided. The winding is the riskiest component in

terms of thermal behavior. Low effective radial thermal conductivity and high loss density of the winding challenge thermal management. The direct solution to resolve this issue is to improve winding effective radial thermal conductivity and layer thermal contact resistance. Both of these solutions depend on manufacturing capability and material properties.

The third challenge is to minimize losses. Fundamental physical principles indicate that motor losses are generated mostly by viscous friction during molecule/electron movements. Higher electrical frequency leads to greater movement of electrons and magnetic dipoles, and eddy current loss. High rotating speed causes more viscous friction in the air. Usually, viscous friction is transformed into heat, which is undesired for motor performance. Minimization of motor loss can lower thermal management stress directly. Motor loss is determined by machine topology inherent characteristics, material properties, electric loading, speed, etc. Coupling EM and thermal effects can improve motor design in terms of efficiency, and electrical and thermal performances.

Both the stator and the rotor generate a large amount of heat. The heat produced by the rotor is dominated by the outer-rotor and the gap windage losses, as discussed in Chapter 4. It is removed by the outer-surface high-speed air mass flow due to the rotor rotation. By contrast, the stator is within the rotor, not contacting the outside ambient air. Therefore, there is a need to pump air through the stator cooling channels. The heat transfer coefficient estimation and the thermal equivalent circuit are described in detail below.

6.2 Heat Transfer Coefficient Estimation

The heat transfer coefficient indicates how effectively fluids remove heat from the interface layer due to convection. Since the rotor spins at high speed, air speed in the gap is quite high and can form turbulent flow easily, which enhances forced convection effects. The front centrifugal fan creates a pressure drop across the gap inlet and outlet to move warm air axially toward outlet holes. In order to simplify the problem, several assumptions are made.

1. Axial flow effect is not considered because its speed is negligible compared with tangential flow speed.

2. Air physical properties are uniform across the whole gap surface.

3. Air physical properties are selected at average air temperature based on inlet and outlet conditions.

4. Rotor and stator surfaces are perfectly smooth. Friction effects are not quantified here.

Tangential flow is dominant and its convection coefficient is estimated with selected empirical correlation from [15]. The Taylor number in the gap is usually defined as

$$Ta = \omega^2 R\delta^3/\upsilon^2 \tag{6.1}$$

where ω is rotating speed, R is stator outer radius, and υ is air kinetic viscosity.

The Nusselt number correlation in the gap between the concentric cylinders is

$$Nu = 0.42(Ta \cdot Pr)^{0.25} \tag{6.2}$$

where Pr is the Prandtl number determined by air physical properties. The corresponding average gap heat transfer coefficient can be estimated as

$$\overline{h_{gap}} = \frac{2\overline{Nu} \cdot k}{\delta} \tag{6.3}$$

The heat transfer coefficient associated with cooling channel surfaces is another important forced convection component. Following are the assumptions in estimating the heat transfer coefficient in cooling channels:

1. Axial flow speed is the same across the whole cooling channel surface.

2. The heat transfer coefficient for rectangular geometry is equivalent to that for round geometry with equivalent hydraulic diameter.

3. Air physical properties are uniform everywhere in the cooling channel.

4. Air physical properties are selected at average air temperature based on inlet and outlet conditions.

5. The heat sink surface is perfectly smooth.

The most common way to estimate the heat transfer coefficient in rectangular cooling channels is to use the heat transfer coefficient estimation method in round cooling channels/pipes. Hydraulic diameter (D_h) is used to convert rectangular geometry to equivalent round geometry cases. The Reynolds number of a round pipe with hydraulic diameter is

$$Re_{Dh} = U_{av} D_h / \upsilon \tag{6.4}$$

where U_{av} is average axial flow in cooling channels, and υ is kinetic viscosity of air.

The friction coefficient (f) and the Nusselt number (Nu) correlation in the cooling channel are given as [16], [17]:

$$f = \frac{1}{(1.82 log_{10}(Re_{Dh}) - 1.64)^2} \tag{6.5}$$

$$\overline{Nu_D} = \frac{(f/8)(Re_{Dh} - 1000)Pr}{1 + 12.7\sqrt{f/8}(Pr^{2/3} - 1)} \tag{6.6}$$

where Pr is Prandtl number determined by air physical properties. Only the average Nusselt number can be obtained here. Due to different geometry and unstable flow dynamics, convection effects at each edge or corner might deviate.

The corresponding average heat transfer coefficient in the cooling channel can be estimated by

$$\overline{h_{hs}} = \overline{Nu_D} \frac{k_{flow}}{D_h} \tag{6.7}$$

where k_{flow} is the flow thermal conductivity. In our case, flow is cooling air. The average velocity of axial air flow determines the heat transfer coefficient of the cooling channels and the outlet temperature. In the baseline design, cooling flow axial speed has to be at least 20 m/s to achieve sufficient convection capability. Coolant mass flow has to be at least 0.6 lbs/sec.

6.3 2-D Thermal Equivalent Circuit

With heat loads and heat transfer boundary conditions estimated, the next step is to predict thermal performance of the proposed design. Usually, CFD and FEM are applied to accurately predict the temperature distribution of

a motor. However, these methods cause huge computational and modeling complexity due to complicated fluid dynamics and structures. A simplified thermal model can be employed to improve computation efficiency at the expense of some accuracy at the initial sizing stage.

As discussed before, the winding has the highest risk of overheating due to its poor radial thermal conductivity, high loss density and obstacles to access cooling flow directly. The rotor is less likely to cause hotspot temperature. Also, it has been found that the radial heat flow is dominant and the hotspot temperature occurs at the outlet end-winding region according to detailed steady state thermal analysis. For simplification, it is sufficient to model the stator 2-D thermal equivalent circuit. The 2-D thermal equivalent circuit of the stator is presented in Figure 6.2.

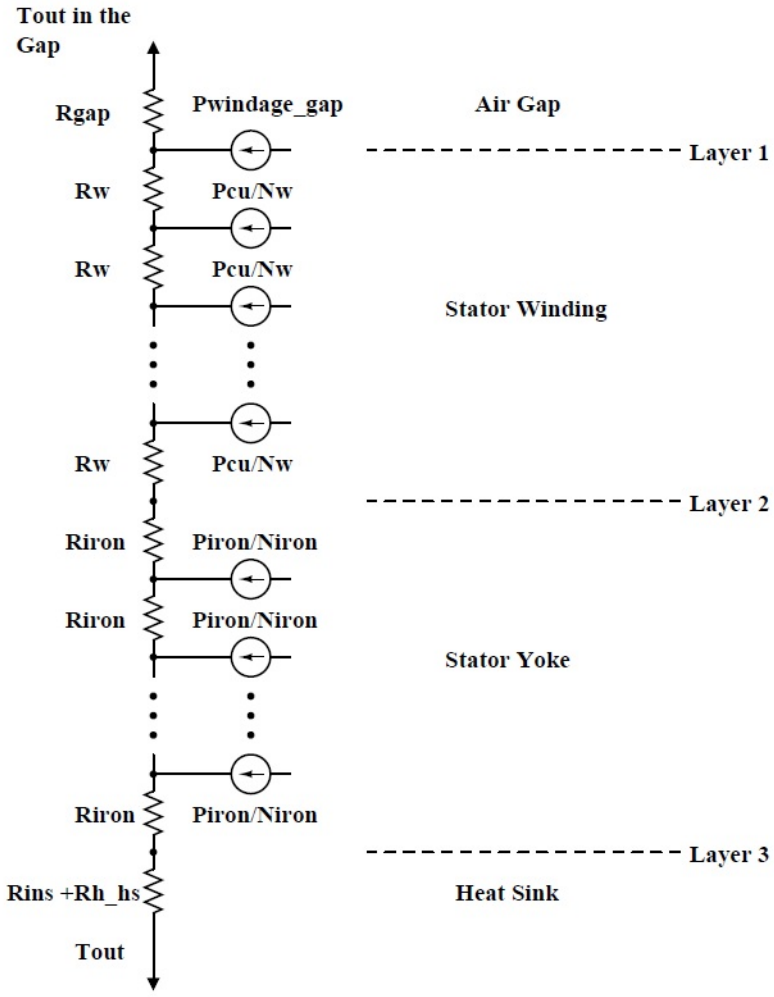

Figure 6.2: 2-D Thermal Equivalent Circuit in Stator

Stators mainly comprise four regions: air gap, stator winding, stator yoke and heat sink. Winding and yoke regions are further decomposed into N_w+1 and $N_{iron}+1$ components. The goal of constructing an equivalent thermal circuit is to calculate unknown temperature potential at each defined node. In the circuit shown in Figure 6.2, total number of nodes assigned is $3+N_w+N_{iron}$ at boundary layers, and injected heat loss source locations. The node index is denoted as i in the whole thermal equivalent circuit analysis.

In the stator winding region, the temperature potential node index is characterized as

$$i_w = \{2, ..., (1 + N_w)\} \tag{6.8}$$

In the stator yoke region, the temperature potential node index is characterized as

$$i_{iron} = \{(3 + N_w), ..., (N_{sy} + N_w + 2)\} \tag{6.9}$$

At interface layers, the temperature potential node index is given as

$$i_{layer} = \{1, (N_w + 2), (N_w + N_{sy} + 3)\} \tag{6.10}$$

With node specification, thermal resistance shares the same index defined in the temperature node index. However, resistance specifications of different indexes vary. From top to bottom in Figure 6.2, the thermal resistance in the gap region (R_{gap}) is derived as

$$R_1 = R_{gap} = \frac{1}{h_{gap} A_{gap}} \tag{6.11}$$

where h_{gap} is the gap heat transfer coefficient and A_{gap} is the stator outer surface area.

Thermal resistance in the winding region (R_w) is given as

$$R_w = ln(\frac{R_{os} - d_{winding} \cdot \frac{i-2}{N_w}}{R_{os} - d_{winding} \cdot \frac{i-1}{N_w}})/(2\pi k_{winding}) \tag{6.12}$$

where R_{os} is the stator outer radius, $d_{winding}$ is the winding slot depth, and $k_{winding}$ is the winding equivalent radial thermal conductivity.

Thermal resistance in the stator yoke region (R_{iron}) is given as

$$R_{iron} = ln(\frac{R_{sy} - d_{sy} \cdot \frac{i-3-N_w}{N_{iron}}}{R_{sy} - d_{sy} \cdot \frac{i-2-N_w}{N_{sy}}})/(2\pi k_{iron}) \tag{6.13}$$

where R_{sy} is the stator yoke outer radius, d_{sy} is the stator yoke depth, and k_{iron} is the iron yoke radial thermal conductivity.

Thermal resistance in the heat sink region is

$$R_{N_w+N_{sy}+4} = R_{ins} + R_{hs} = \frac{t_{ins}}{A_{ins}k_{ins}} + \frac{1}{h_{hs}A_{hs}} \tag{6.14}$$

where t_{ins} is the insulator thickness, A_{ins} is the insulator layer surface area, h_{hs} is the heat sink average heat transfer coefficient, and A_{hs} is the heat sink total effective cooling area

Then, thermal admittance matrix G entries can be specified as follows:

$$G_{i,i} = \frac{1}{R_i} + \frac{1}{R_{i+1}} \tag{6.15}$$

$$G_{i,(i+1)} = G_{(i+1),i} = -\frac{1}{R_{i+1}} \tag{6.16}$$

The thermal resistance index and its associated resistance are specified in Equations 6.8—6.14.

The heat source vector is given as

$$P_i = \begin{cases} P_{windage\_gap} + T_{out}/R_{gap} & \text{if } i = 1 \\ P_{cu}/N_w & \text{if } i \in i_w \\ P_{iron}/N_{sy} & \text{if } i \in i_{sy} \\ T_{out}/(R_{hs} + R_{ins}) & \text{if } i = N_w + N_{sy} + 3 \\ 0 & \text{otherwise} \end{cases} \tag{6.17}$$

according to physical relations presented in Figure 6.2.

The unknown temperature potentials at defined nodes in the stator thermal equivalent circuit can be solved by applying network analysis principles. The thermal network equation is given by

$$[G][T] = [P] \tag{6.18}$$

where $[G]$ is the admittance matrix in the equivalent circuit, $[T]$ is the unknown temperature potential vector, and $[P]$ is the injected heat source vector.

The advantages of such an equivalent circuit method are robustness of estimation accuracy by defining preferred temperature node number, and efficiency of predicting machine hotspot temperature with given design specifications. The disadvantage is lack of axial heat flow consideration. Currently, it is assumed that no heat flows in the axial direction, because there is a possibility that the end-winding cooling effect is sufficient that end-winding heat does not flow back to the active region. Without further end-winding region fluid analysis or rotor bench test result, it is hard to predict flow behavior and its effects on hotspot temperature.

6.4 Finite Element Analysis Verification

2-D steady state thermal analysis was conducted to verify thermal equivalent circuit accuracy. The baseline design is specified in Table 3.1. Exactly the same dimensions, boundary conditions, heat sources and thermal physical properties were applied in both thermal analysis methods.

The results of the simplified 2-D thermal equivalent circuit and FEM analyses are summarized in Table 6.1. The stator temperature prediction of the

Table 6.1: Stator Temperature Prediction Comparisons with FEA

Temperature	FEA	Analytical	Error
T1	140	147.07	5.05%
T2	138.5	147.14	6.22%
T3	132.4	144.36	9.07%
T4	126.6	138.67	9.52%
T5	119	130	9.27%
T6	117.1	128.33	9.64%

thermal equivalent circuit is consistent with the FEA result. The hotspot temperature prediction error is around 5%. However, the largest temperature prediction error is around 10%. Due to the different sizes of lumped components, the temperature prediction accuracy varies at different nodes. In this

case, the winding region is divided into four components with equal depth. By contrast, the stator iron region is divided into only two components.

To improve accuracy, more temperature nodes need to be specified in the dense heat loss region, such as winding and iron region. If the heat loss source increases, temperature prediction deviation will rise accordingly, which might cause non-negligible uncertainties in overall machine sizing when performing multi-physics optimization. A reasonable node number should be assigned to keep uncertainties in temperature prediction within a desired range.

CHAPTER 7

CONCLUSIONS AND FUTURE WORK

A 1 MW high-frequency air-core permanent magnet motor design for aircraft electrification was presented. It is targeted for achieving power density over 13.3 kW/kg, which is around 2-4 times the current-of-the-state-art. Detailed machine topology and structure configuration design considerations were presented and discussed. While such a novel electrical machine concept increases the possibility of replacing conventional aircraft engines, there are many challenges in pushing the power density of the machine. Conventional machine design methods heavily rely on finite-element-method software, which provides accurate performance prediction but is time-consuming in sizing optimization. Furthermore, current machine design software does not cover our novel topology and inconveniently requires extra customized modeling set-up. An alternative method is to develop electromagnetic and thermal analytical models of this proposed motor.

In order to facilitate future large-scale multi-physics optimization of this proposed motor topology, rigorous electromagnetic and thermal analytical models were developed in this thesis. Electromagnetic modeling was derived from fundamental Maxwell's equations with around 2% error in flux distribution prediction and 5% error in torque estimation. It is a competitive machine design method in terms of quick initial sizing and large-scale multi-physics optimization.

In addition to EM modeling, another important aspect of machine design, especially in raising machine power density, is thermal modeling. Detailed heat load estimation methods for copper loss, iron loss and mechanical loss were presented and partially verified with FEA results. A critical winding equivalent thermal conductivity quantification method was derived and verified with a bench test. In addition, a 2-D thermal equivalent circuit coupled with detailed heat load analysis was developed to detect hotspot temperature quickly and accurately. Simplified temperature prediction analytical

modeling was also verified initially with FEA results.

For future work, EM modeling needs more generalized analytical solution in terms of segmented Halbach PM array. Harmonic effects of the magnetic field are not accounted for at this stage, which might cause underestimation of AC loss and iron loss. Average torque prediction accuracy needs improvement. Maybe important lumped electrical parameters, such as phase inductance, can be derived accordingly to facilitate future drive system design and optimization. Thermal analysis needs more bench test verification, especially fluid dynamic aspects which determine most mechanical losses and heat transfer effects. The 2-D thermal equivalent circuit might not be sufficient to accurately predict hotspot temperature in some cases. The thermal analysis should be extended to a 3-D thermal analytical model either by lumped component method or by solving the partial differential equation to account for axial heat flow effects. Thermal analysis also needs further accuracy improvements in both loss estimation and temperature prediction. Last, developed EM and thermal models with decent accuracy should be applied to a large-scale multi-physics optimization to find an optimal machine sizing with the highest power density and adequate efficiency.

REFERENCES

[1] National Aeronautics and Space Administration, "Advanced air vehicles program, advanced air transport technology project," September 2014, fixed Wing/Advanced Air Transport Technology Project Overview, NRA Kick-off Meeting, Cleveland, OH.

[2] M. Hathaway, R. Rosario, and N. Madavan, "NASA fixed wing project propulsion research and technology development activities to reduce thrust specific energy consumption," in *49th AIAA/ASME/SAE/ASEE Joint Propulsion Conference*, 2013.

[3] C. Luongo and et al., "Next generation more-electric aircraft: A potential application for HTS superconductors," *IEEE Transactions on Applied Superconductivity*, vol. 19, no. 3, pp. 1055–1068, 2009.

[4] J. Motors, "Introducing the JM1S motor." [Online]. Available: http://www.jobymotors.com/public/views/pages/products.php

[5] N. Madavan, "Hybrid electric propulsion systems: the NASA FW/AATT project perspective," in *Fixed Wing Project Fundamental Aeronautics Program*, 2014.

[6] T. Lipo, *Introduction to AC Machine Design*. University of Wisconsin–Madison, 2011.

[7] X. Zhang and K. Haran, "High high-specific-power electric machines for electrified transportation applications technology options," in *Energy Conversion Congress and Exposition (ECCE)*, 2016.

[8] A. Yoon, X. Yi, J. Martin, Y. Chen, and K. Haran, "A high-speed, high-frequency, air-core PM machine for aircraft application," in *Power and Energy Conference at Illinois (PECI)*, 2016.

[9] Z. Xia, Z. Zhu, and D. Howe, "Analytical magnetic field analysis of Halbach magnetized permanent magnet machine," *IEEE Transactions on Magnetics*, vol. 40, no. 4, pp. 1864–1872, 2004.

[10] X. Tang and C. Sullivan, "Stranded wire with uninsulated strands as a low-cost alternative to Litz wire," in *Power Electronics Specialists Conference*, 2004, pp. 854–860.

[11] G. Bertotti and M. Pasquale, "Physical interpretation of induction and frequency dependence of power losses in soft magnetic materials," *IEEE Transactions on Magnetics*, vol. 28, pp. 759–766, 1992.

[12] P. Childs, *Rotating Flow*. Butterworth-Heinemann, 2010.

[13] J. Vrancik, "Prediction of windage power loss in alternators," NASA Technical Note, Tech. Rep., 1968.

[14] L. Dorfman, *Hydrodynamic Resistance and the Heat Loss of Rotating Solids*. Oliver & Boyd, 1963.

[15] Y. Yamada, "Resistance of a flow through an annulus with an inner rotating cylinder," *JSME*, vol. 5, no. 18, pp. 302–310, 1961.

[16] B. Petukhov, "Transfer and friction in turbulent pipe flow with variable physical properties," *Advances in Heat Transfer*, vol. 6, pp. 504–564, 1970.

[17] V. Gnielinski, "New equations for heat and mass transfer in turbulent pipe and channel flow," *Int. Chemical Engineering*, vol. 16, pp. 359–368, 1976.